Tailoring Material and Mechanochemical Responses with Microstructure

Morgan Bassford

A thesis
submitted in partial fulfillment of the
requirements for the degree of

Master of Science in Mechanical Engineering

University of Washington

2017

Committee:

Nicholas Boechler, Chair

Mark Ganter

AJ Boydston

Program Authorized to Offer Degree:
Mechanical Engineering

University of Washington

Abstract

Tailoring Material and Mechanochemical Responses with Microstructure

Morgan Bassford

Chair of the Supervisory Committee:
Assistant Professor Nicholas Boechler
Mechanical Engineering

The objectives of this project were twofold: (i) to develop a methodology for tailoring the nonlinear elastic response of a 2D lattice material through designed microstructural geometric nonlinearities; and (ii) to show that activation of mechanophores (such as spiropyran) can be similarly manipulated through lattice geometry. Exploring this space may lead to new materials that can be engineered to yield prescribed mechanical and chemical loading responses, such as dissipating or focusing energy when struck or triggering chemical reactions under certain loads. The ability to customize these properties in a systematic way could facilitate the design and fabrication of advanced energetic, impact-mitigating, self-healing or self-reinforcing materials.

In this thesis, a heuristic exploration of 2D nonlinear lattices was conducted, in which lattices were designed, modeled in COMSOL, and then 3D printed and quasi-statically tested to validate simulation results. A lattice that softens under compression, as well as two that stiffen under compression (using contact and non-contact based mechanisms) were created. A nonlinear topology optimization scheme using a MATLAB genetic algorithm and COMSOL Finite Element Analysis (FEA) was also created to find structures to match prescribed force-displacement curves: however, this topology optimizer struggled finding non-unique solutions

and poorly connected structures. Spiropyran was embedded in PDMS and studied in quasi-static and dynamic compression. It was found that spiropyran activated at compressive strains greater than 0.7 at both high and low strain rates and in less than 8 ms during dynamic tests. Finally, spiropyran was embedded in PCL and printed into an oval pore lattice shape; these samples, as well as control (non-lattice, bulk) samples were subjected to tensile tests. As spiropyran activation in the lattices was observed prior to activation in the control samples, these experiments suggest that microstructure can amplify mechanochemical response.

TABLE OF CONTENTS

LIST OF FIGURES

ACKNOWLEDGMENTS

My thesis could not have been put together without significant help from others. For their considerable efforts on the nonlinear lattices portion of this project, I would like to acknowledge Suraj Bhosale, Ariana Mendible, Tim Brummer and Sam Merritt. Suraj was integral to the early the lattice ideation and validation phase of the project, while Ariana, Tim and Sam contributed essential code, ideas and strategies to the nonlinear topology optimization sections of this thesis.

Characterization of spiropyran in PDMS could not have been achieved without significant help and wisdom from Johanna Schwartz (who also manufactured the spiropyran) and Courtney Shaeffer, who assisted in carrying out most of the quasi-static experiments as well as contributed her photography knowledge to set up the lighting for these tests. Maroun Abi Ghanem was also an invaluable resource in setting up and conducting the high speed camera experiments.

Within the Boechler group, I thank Sam Wallen, Morgan Hiraiwa and Amey Khanolkar for welcoming me to the research team and helping me use lab resources or battle LaTeX formatting.

I would also like to thank my committee, Professors Nicholas Boechler, Mark Ganter and AJ Boydston, for giving me valuable feedback and being incredibly flexible regarding my presentation and thesis schedule. I thank Professor Vipin Kumar for encouraging me to attend the University of Washington as well as encouraging me to take his masters projects class, which eventually spun into this thesis. Finally, I thank Professor Boechler again for supporting me and guiding me in this project as an involved advisor.

DEDICATION

I dedicate this thesis to my parents, who taught me to value my education.

Chapter 1
INTRODUCTION

1.1 Project Overview

The broader objective of this project was to establish new methods for creating responsive, adaptable material systems. Such engineered materials could be tailored to have mechanical and/or chemical characteristics such as dissipating or focusing energy when struck, releasing substances at critical stresses, or undergoing chemical change in certain loading conditions. The ability to customize these properties in a systematic way would thus facilitate the design and fabrication of advanced energetic, impact-mitigating, self-healing or self-reinforcing materials. Within this context, this thesis studies engineered materials from two perspectives: (i) tailored effective material nonlinearity stemming from designed microstructural geometric nonlinearities, and (ii) amplification of mechanophore activation through microstructure.

Manipulating structural nonlinearities enables the creation of materials that have prescribed loading responses. In granular media, the contact between particles results in a geometric nonlinearity that manifests as a nonlinear elastic material response [1], illustrating how microstructure can influence the overall medium's "effective" properties. Similarly, in lattice metamaterials, which are comprised of small, tessellating unit cells, the geometry of the unit cell determines the overall material response of the structure: changing the connectivity, shape or composition of the unit cell markedly alters the global material characteristics of the lattice [2]. This engineered nature of lattice metamaterials and the availability of high-precision, reliable 3D printing enables the exploration of how geometric nonlinearities on the unit cell level can be used to create prescribed nonlinear material responses on the macroscopic lattice scale. Initial investigation of tailoring nonlinearity in structures can be

seen with Jutte and Kota designing 1D nonlinear springs [3] as well as Ma *et al.* creating a 2D lattice structure that stiffens under tension to match the behavior of skin [4]. Wang, Sigmund and Jensen developed a method for creating truss-based and continuum materials to match prescribed stress-strain curves and Poisson's ratios, respectively [5].

The embedding of mechanically-activated molecules—"mechanophores"—into materials also has been shown to enable new types of material adaptability and responsivity. Spiropyran is one such mechanophore that changes color when subjected to extreme strain [6]. Spiropyran activation can be seen quasi-statically (in PDMS) [7], at high strain rates (in PMMA) [8], and can even be 3D printed into structures [9]. Mechanophores have also been shown to enable the release of small organic molecules under compression [10] or enact material-strengthening reactions during shear loading [11]. Nevertheless, the influence of metamaterial geometry on mechanophore activation remains unexplored, although studies of natural materials suggest that mechanochemistry and microstructure are often intertwined in many nature [12]. As suggested previously, many potential applications of these new materials are in dynamic contexts. Not only does the interplay between mechanochemistry and microstructure need further exploration, the dynamic response of such underlying mechanochemically responsive polymers must be studied.

To begin developing a methodology for tailoring the nonlinear elastic response of a 2D lattice metamaterial and to show that activation of mechanophores (such as spiropyran) can be similarly manipulated through lattice geometry, this thesis seeks to answer these three questions:

1. **How can microstructural geometric nonlinearity be used to tailor lattice metamaterials to result in any nonlinear elastic response?**

2. **How fast does mechanophore activation occur?**

3. **How can microstructural lattice geometry enhance mechanophore activa-**

tion?

1.2 Thesis Organization

This thesis is organized into six chapters. The first part of this work is dedicated to investigating tailored metamaterial nonlinearity and thus answering Question 1 laid out in Section 1.1 above.

- Chapter 2 describes a heuristic design process used to find 2D lattice geometries that stiffen and soften under prescribed displacement loading in tension and compression. Samples were designed using the Structural Mechanics module in COMSOL, 3D printed from a compliant rubber, and then compressed using an Instron load frame to validate simulated stiffening/softening responses.

- Chapter 3 describes a topology optimization code developed to start computationally designing nonlinear lattice geometries. This topology optimization code uses a MATLAB genetic algorithm working in tandem with COMSOL FEA to identify structures to match pre-set prescribed load-displacement curves.

The second part of this work addresses Question 2 from Section 1.1 and discusses characterizing the chosen mechanophore, spiropyran.

- Chapter 4 describes the quasi-static behavior of spiropyran in a 15:1 mixture of polydimethylsiloxane (PDMS) and finds that activation for spiropyran in this polymer occurs at about 0.7 compressive strain.

- Chapter 5 describes the dynamic behavior of spiropyran in a 15:1 mixture of PDMS and finds activation of spiropyran occurs within 8 ms of a 25 x 25 x 35 mm sample being struck at 11.5 m/s. This chapter also discusses local spiropyran activation triggered using a point load of 7.56 kg moving at 1.7 m/s.

The final chapter addresses the influence of lattice microstructure on mechanophore activation and thereby explores Question 3 from Section 1.1.

- Chapter 6 describes the creation of oval and Kagome lattices out of spiropyran-containing 10:1 PDMS or 3D printed polycaprolactone (PCL). These structures are compressed or pulled apart and early activation is seen in an oval lattice printed out of PCL under tension.

Chapter 2

HEURISTIC EXPLORATION OF NONLINEAR LATTICE GEOMETRIES

2.1 Objective

As introduced in Chapter 1, exploring nonlinear lattice structures can be a large component of creating an adaptable, responsive material system. Consequently, both this chapter and Chapter 3 are dedicated to answering the question: **how can microstructural geometric nonlinearity be used to tailor lattice metamaterials to result in any nonlinear elastic response?**

In this chapter, initial investigations into creating nonlinear lattice structures are discussed. Structures were created to stiffen or soften under quasi-static compression to develop understanding of which microstructures yield certain overall material behaviors, as well as show how geometric nonlinearity alone can determine global nonlinearity of a metamaterial structure.

2.2 Literature Review

2.2.1 Bend- and Stretch-Dominated Structures

Lattice structures, comprised of small, regularly patterned strut-based unit cells, can be considered to be materials in that they have their own effective material properties [2]. These structures/materials are often referred to as structural "metamaterials"—materials that have "certain mechanical properties defined by their geometry rather than their composition" [13]. Lattice metamaterials are often classified as bend- or stretch-dominated, designations that

are determined by unit cell geometry and describe the overall characteristics of the medium.

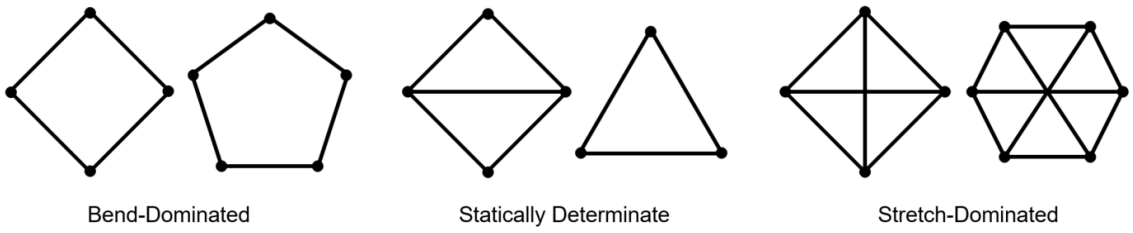

Figure 2.1: Classification of different unit cells.

Whether a lattice is bend- or stretch dominated is determined via Maxwell's stability criterion, which in 2D is:

$$M = b - 2j + 3 \tag{2.1}$$

where b is the number of struts in the unit cell and j is the number of joints in the unit cell (Figure 2.1) [2]. Structures with $M < 0$ are bend-dominated; if the unit cell were to have pinned joints instead of fixed ones, the unit cell becomes a mechanism that would collapse under loading. In contrast, unit cells with $M > 0$ are over constrained and stretch-dominated, meaning that they would be self-supporting under load even with pinned joints [2]. For $M = 0$, the structures are statically determinate—they contain the minimum number of internal constraints to prevent movement of the structure under loading with pinned joints and are still classified as stretch-dominated structures [2]. Bend-dominated structures are called such because in the context of a structural lattice, they carry load in the bending of around the joints of their unit cells, while stretch-dominated structures carry the load in tension and compression of its internal struts [14]. Bend-dominated structures have been shown to absorb energy well, while stretch-dominated structures can be extremely stiff and lightweight [2].

2.2.2 Structural Lattices

A recent focus in lattice metamaterials research has been on creating materials that are extremely stiff at low densities. Li *et al.* modeled and experimentally studied the collapse mechanisms of body centered cubic (BCC) metal lattices created via selective laser melting, noting that loading this (bend-dominated) structure resulted in stress localized around the connective nodes in the lattice, creating plastic joints connected by primarily elastic beams [15]. Smith *et al.* studied similarly manufactured BCC and BCC-Z structures, finding that the more constrained BCC-Z structure is far stiffer than the BCC configuration, especially at low relative densities [16]. Schaedler *et al.* created extremely low-density microlattices capable of recovering their shape after loading. Furthermore, the stiffness of these lattices (E) scaled with density (ρ) according to $E/E_s = (\rho/\rho_s)^2$ (the subscript "s" indicates the properties of the source material), which matches the stiffness scaling of lightweight foams. [17]. Zheng *et al.* manufactured other low-density microlattices using the extremely over constrained (and consequently stretch-dominated) octet truss unit cell geometry, finding that their structures scaled with density close to the theoretical maximum of $E/E_s = \rho/\rho_s$ [13].

2.2.3 Nonlinear Structures

The lattices described in Section 2.2.2 are largely designed to be as stiff or energy absorbing as possible at low relative densities. However, manipulation of nonlinearity in structures has also been explored, although to a lesser extent in lattices. Jutte and Kota used a genetic algorithm to create 1D springs to match prescribed load-displacement functions, such as J- or S-curves at large displacements [3]. Ma *et al.* designed a 2D "horseshoe" lattice that stiffens in a J-curve under tension in order to match the behavior of skin [4]. Jutte's and Ma's studies use geometric nonlinearity to supply the global nonlinear behaviors of their structures, while Haghpanah *et al.* showed that lattice connectivity could control lattice stiffness and Poisson's ratio [18]. Furthermore, Overvelde and Bertoldi demonstrated that

Poisson's ratio and global buckling behavior in periodic porous structures can be determined by pore shape [19]. In the dynamic regime, Fraternali modeled wave propagation through periodic tensegrity structures, observing that the wave dynamics could be heavily influenced by pre-tensioning the strings in the structures [20] and Raney *et al.* examined high fidelity wave propagation in a bistable one-dimensional lattice structure [21].

2.3 Design Process and Constraints

2.3.1 Design Space

For initial exploration of nonlinear lattices, the design space was constrained in order to produce meaningful progress over the length of this project (four quarters). Consequently, the research focus was narrowed to designing 2D lattices that exhibited nonlinear behavior under quasi-static compression loading (Figure 2.4). Compression was chosen over tension since platens are much easier to setup and provide better boundary condition control than jaws during experimental testing (Figure 2.5). In addition to being the logical starting point before conducting dynamic tests, studying lattice behavior quasi-statically also made for more simple characterization, as quasi-static tests do not require numerous unit cells or advanced imaging equipment to capture lattice behavior.

With strain rate and testing method decided, additional geometric constraints were placed on lattice geometries during to ensure that structures would in fact be *lattices* as well as permit repeated loading attempts. Consequently, any proposed models for lattice structures had to:

1. Employ geometric, not material, nonlinearities to meet the constitutive laws as described in Figure 2.2.

2. Not fail via buckling to ensure repeated behavior in simulation and experiments.

3. Be symmetric along two axes.

4. Be comprised of tessellating unit cells.

With the above constraints in mind, various lattice geometries were developed to soften and stiffen in tension and compression as shown in Figure 2.2. We aimed to identify microstructural mechanisms that result in these qualitative classes of nonlinear response. The designed structures that result in these various load-displacement (or stress-strain) curves are displayed in Figure 2.2 and discussed in more detail in the following sections.

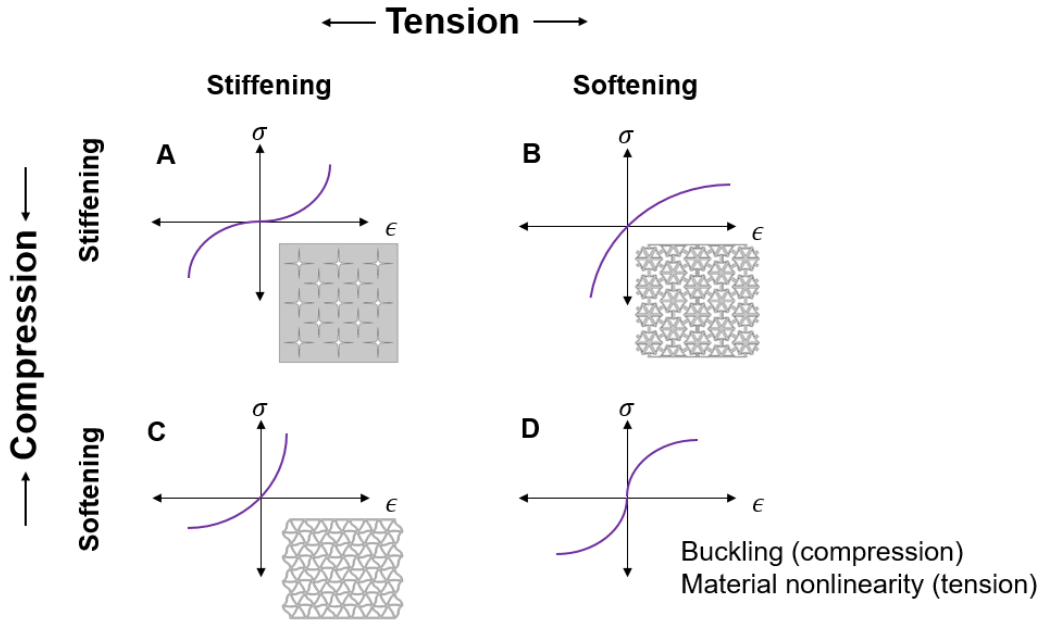

Figure 2.2: The design space for lattice structures is broken down into different categories based on stiffening or softening behavior under tension and compression. Note that in quadrant D, softening in tension and compression is theorized to occur only through a combination of buckling and material nonlinearity.

2.3.2 Lattice Ideation

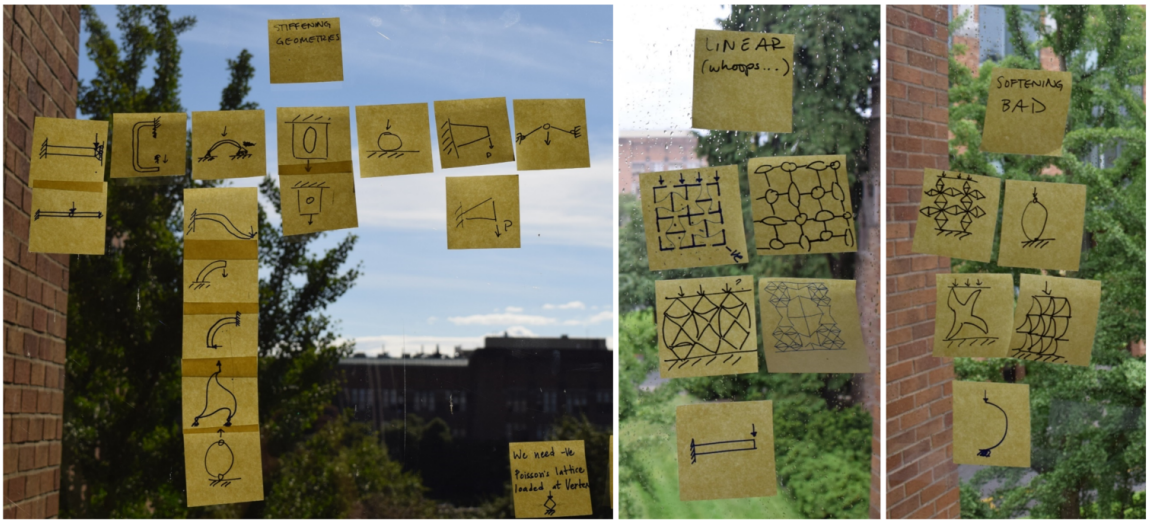

Figure 2.3: Brainstorming of some compression-stiffening geometries.

Design of the lattices was an iterative process, whereupon many structures that fit the constraints listed in Section 2.3.1 were sketched, discussed within the group[1] and then modeled/parametrized in COMSOL Multiphysics (discussed in greater detail in Section 2.4) to evaluate their global nonlinear behavior.

During the design process it was observed that designing structures that soften under compression is fairly trivial, as structures with little material, low connectivity or excessive beam bending all typically have some sort of softening behavior. Softening could be enhanced by designing a structure comprised of curved beams that get progressively more bent under loading, a phenomenon exploited by the lattice in Section 2.5.1.

In contrast, developing a lattice that stiffens under compression within the constraints previously set proved more challenging. For these structures, the design process began with considering simple cases of geometric nonlinearity that lead to stiffening as are listed here

[1]The author would like to acknowledge the work of Suraj Bhosale (ITT-Gandhinagar) here, who contributed significantly to the brainstorming and COMSOL modeling efforts of this project.

(Figure 2.3, left):

- Curved beams that are forced to straighten
- Tapered beams that are fixed and loaded perpendicular to the taper
- Beams that are constrained at both ends
- Pre-snap through structures
- Sphere contact (Hertz contact)
- Stretching of bulk materials with cylindrical/ellipsoid shapes cut out

From this list of simple shapes, various unit cells were assembled and then patterned into lattice structures for simulation in COMSOL. Two lattices developed via this method are discussed in the following sections. Furthermore, through this process it was observed that non-contact mechanisms that stiffen under compression provide softening under tension and vice versa.

2.4 Experimental Validation

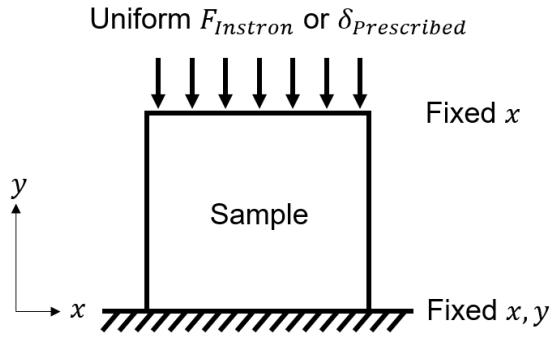

Figure 2.4: Loading conditions for comparison between simulated and experimental results.

As mentioned above, the proposed lattice geometries were designed in COMSOL Multiphysics 5.2a with the Structural Mechanics module. Two-dimensional lattice geometries were created using the built in COMSOL geometry tools, with important dimensions such as beam thickness, beam curvature, number of unit cells and size of unit cells parametrized in COMSOL to better explore the extent of any given nonlinearity. All lattices were simulated in plane strain, used the material properties of TangoBlack (discussed in Section 2.4.2), and were modeled as a linear material. Since lattice geometries were designed to avoid activating material nonlinearity (ex. high strains to induce plasticity), nonlinear material models were avoided to simplify the FEA. The models were meshed with quad elements where possible. Finally, a prescribed displacement and a fixed constraint were applied to the top and the bottom of the lattice (Figure 2.4), respectively. Using a stationary study, the prescribed displacement was then incremented up using a parametric sweep until the model failed via self-contact or buckling with the geometric nonlinearity option on. When a lattice was found to match one of the nonlinear behaviors shown in Figure 2.2, its geometry was varied using the parametrized dimensions and a version of the structure with the most dramatic nonlinearity was printed and tested for model validation.

2.4.1 Experimental Test Setup

Lattices were compressed at 1 mm/min on an Instron 5585H load frame using flat platens. Load and crosshead displacement were recorded with a 50 N load cell and deformation was captured using a Nikon D5600 camera (Figure 2.5).

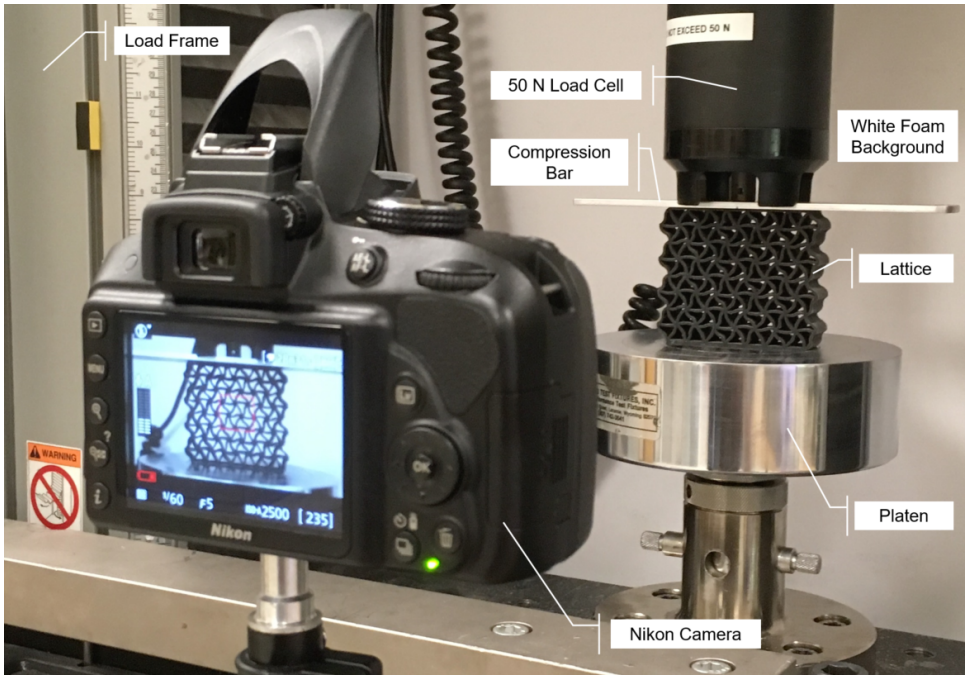

Figure 2.5: Experimental test setup for validating nonlinear lattice behavior.

Due to friction between the lattices and the platens, the top and bottom surfaces of the lattices were observed to be fixed with no sliding in the lateral direction. Consequently, during COMSOL modeling, the top and bottom edges of the simulated lattices were constrained in the x-direction (Figure 2.4).

2.4.2 Material Selection: TangoBlack

The complexity of lattice geometries and expected iterative nature of the design process required that the lattices be created via high resolution additive manufacturing. As a result, lattices were printed on a Stratsys Objet 260 out of TangoBlack, a proprietary "rubber-like" material that is flexible and can undergo high elongation [22]. A highly elastic material, TangoBlack was selected as it would enable repeated testing without activating material nonlinearity, satisfying the constraints for lattices laid out in Section 2.3.1.

TangoBlack was characterized in tension and in compression to 0.1 strain (Figure 2.6). For the tension tests, samples were ASTM D638 Type 1 dogbone specimens, while 1.0 x 3.0 x 3.0 cm cubes were used for testing in compression. Samples were printed in both parallel ("horizontal") and perpendicular ("vertical") orientations at 100% infill with respect to loading.

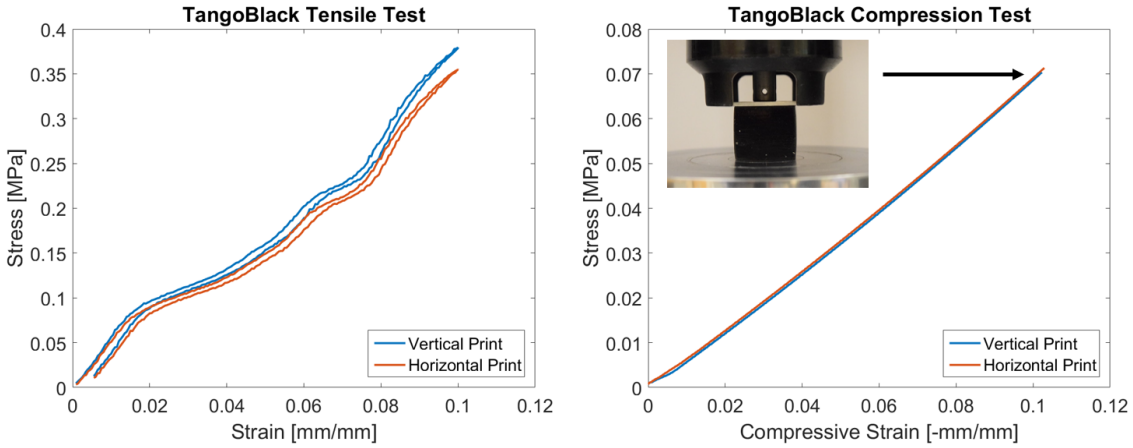

Figure 2.6: Stress-strain diagrams for TangoBlack in compression and tension.

These tests showed that TangoBlack exhibits very little material hysteresis when loaded and unloaded (Figure 2.6, left) and that the print orientation had little affect on the sample material properties, particularly in compression (Figure 2.6, right). In tension, the Young's modulus was about 3.66 x 10^6 Pa, while in compression it was found to be 6.95 x 10^5 Pa. Poisson's ratio was estimated to be about 0.4. The values used in all subsequent COMSOL modeling are given in Table 2.1 below.

Table 2.1: Properties of TangoBlack

Property	Value	Units
Young's Modulus	6.95 x 10^5	Pa
Poisson's Ratio	0.4	-
Density	1.14	g/cm^3

2.5 Developed Lattice Geometries

2.5.1 Compression-Softening Lattice

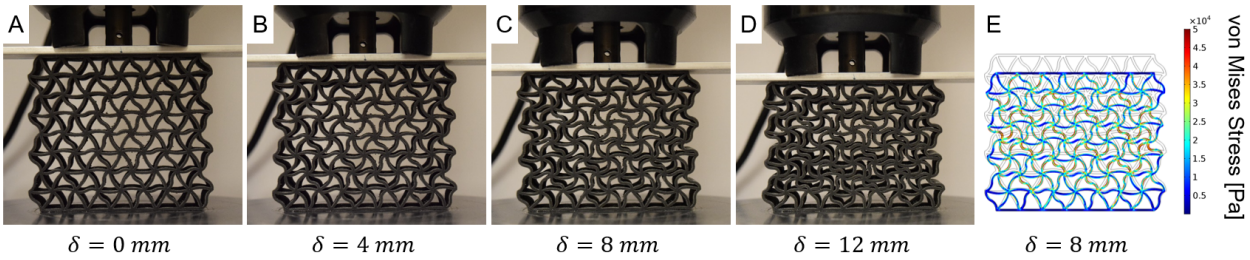

Figure 2.7: Compression of the softening lattice.

A lattice that softens under quasi-static compression was developed (Figure 2.7) that complies with the constraints listed in Section 2.3.1. This lattice, with approximate maximum dimensions of 68 x 70 x 20 mm, was printed in TangoBlack with 1 mm thick curving beams joined in a tessellated triangular pattern inspired by the post-buckled shape of a frustrated straight-beam triangular lattice [23]. As shown in Figure 2.7, its beams bend to become more curved under compression and rotation of the central nodes where the beams are connected enables this bending without buckling.

Figure 2.8: Geometry used to create the softening lattice.

The primary mechanism for softening, the increasingly deformed curved beam, is shown in Figure 2.8. As mentioned above, the lattice is very stable and manages high amounts of deformation due to its high inner connectivity from the triangular patterning. To compare with simulation results, the structure was experimentally compressed on the Instron until densification of the structure occurred near 14 mm.

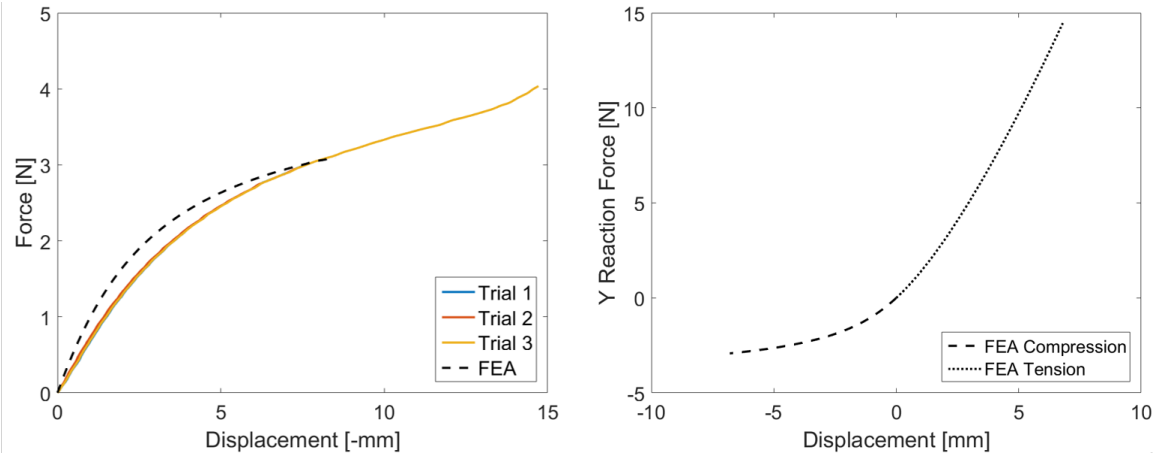

Figure 2.9: Left: Comparison of FEA and experimental data. Force is measured at the load cell. Right: Same lattice simulated in compression and tension. Note that the Y reaction force is measured from the lattice side in the right graph.

As shown in Figure 2.9, the COMSOL simulation produced a reasonable fit to the measured load-displacement curve. The difference between the experiment and FEA data could be attributed to using a linear material model during simulation. As TangoBlack is similar

to rubber, a Neo-Hookean or Ogden material model might more accurately capture the behavior of the material. Finally, simulation of the lattice in tension as well as compression (Figure 2.9) indicates that it is a structure that softens in compression and stiffens in tension using geometric nonlinearity alone, satisfying the "C" quadrant of the design domain (Figure 2.2).

2.5.2 Compression-Stiffening Lattice (Contact)

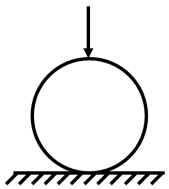

Figure 2.10: Loading a sphere on a flat surface.

A lattice that stiffens under compression was developed using inspiration from porous cellular solids [19] and contact between an elastic sphere and half-space (Figure 2.10). When a sphere is loaded on a flat surface as shown in Figure 2.10, the contact area between the two increases as the surface and/or sphere deform. Consequently, the force required to load the sphere increases nonlinearly [1]:

$$F = \frac{4}{3} E^* r^{1/2} d^{3/2} \tag{2.2}$$

Where E^* relates the moduli of the two materials, r is the radius of the sphere and d is the displacement of the sphere into the plane [1]. Using these concepts, the lattice shown in Figure 2.11 was created with cutouts that close under compression and thus increase resistance to loading at higher displacements. The curves that comprise the edges of each cutout are hyperbolic, leading to a smooth increase in contact during loading.

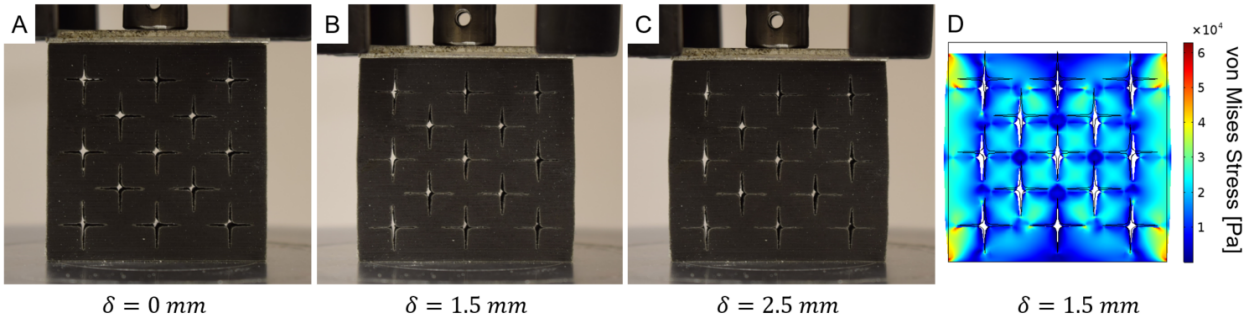

Figure 2.11: Compression of the contact-stiffening lattice.

This contact stiffening lattice, measuring 40 x 40 x 10 mm, was printed in TangoBlack and compressed 2.5 mm on the Instron until the the gaps in the structure closed (Figure 2.11, C). In simulation, (Figure 2.11, D) contact between surfaces was simulated using the augmented Langrangian method and the mesh was refined along contact boundaries in order to encourage the model to converge.

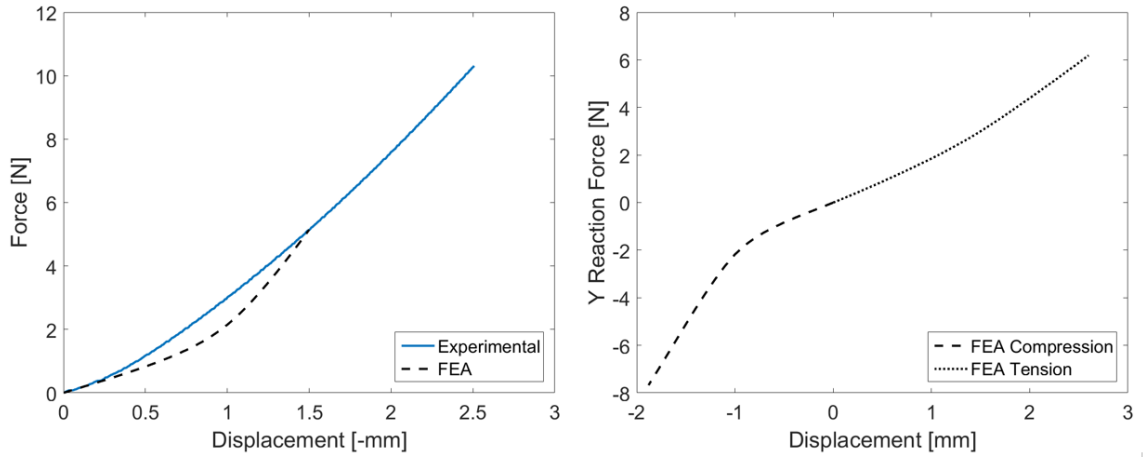

Figure 2.12: Left: Comparison of FEA and experimental data for the contact stiffening lattice. Force is measured at the load cell. Right: Same lattice simulated in compression and tension. Note that the Y reaction force is measured from the lattice side in the right graph.

Experimentally, the lattice showed mildly nonlinear behavior, while the COMSOL model

indicated a more dramatic stiffening after 1 mm of displacment (Figure 2.12, left). The disparity between these data is attributed to complications in both simulation and experimentation. It was observed post test that the gaps in the 3D printed lattice were not completely evacuated of support material. Consequently, there was more material in contact from the beginning of the compression test that was not accurately captured by the COMSOL model. Due to the challenges involved in modeling contact, we note that the simulation fails at 1.5 mm of displacement when elements penetrate each other. To overcome this problem, further refinement of the model or simulation using a different solver (i.e. ABAQUS) is needed.

Nevertheless, the COMSOL FEA model indicates that this lattice will stiffen in tension and compression as the cutouts collapse and increase internal surface area contact (Figure 2.12, right). This satisfies the "A" quadrant in the design domain illustrated in Figure 2.2.

2.5.3 Compression-Stiffening Lattice (Non-Contact)

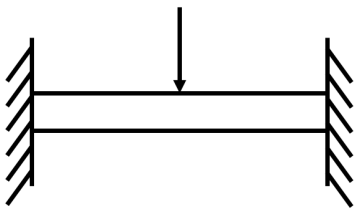

Figure 2.13: Center loading a beam with fixed-fixed end conditions.

Applying a force to the middle of a beam with fixed ends yields a stiffening load-displacement curve (Figure 2.13), and the non-contact stiffening lattice was designed with this structure in mind. Consequently, this lattice does not rely on contact as the mechanism for its stiffening behavior.

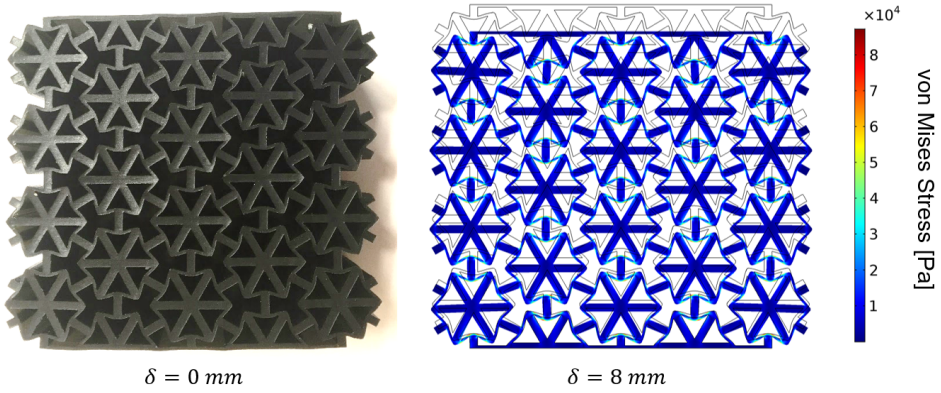

Figure 2.14: Compression of the non-contact stiffening lattice.

As shown in Figure 2.14, the non-contact stiffening lattice consists of hexagonal unit cells that have thick cross members (1.2 mm thick) linked by thin beams of material (0.8 mm thick). Under compression, the thick inner members provided fixed end conditions for the thin beams, imitating the scenario in Figure 2.13 and resulting in an overall stiffening behavior for the lattice. The hexagonal shape provides enough connectivity within the structure to prevent buckling: previous models with quadrilateral unit cells, due to poor connectivity and having elements in parallel with the direction of loading, were shown to buckle in simulation (Figure 2.17). This lattice, approximately 103 x 112 x 30 mm in size, was printed in TangoBlack and compressed 7 mm on the Instron.

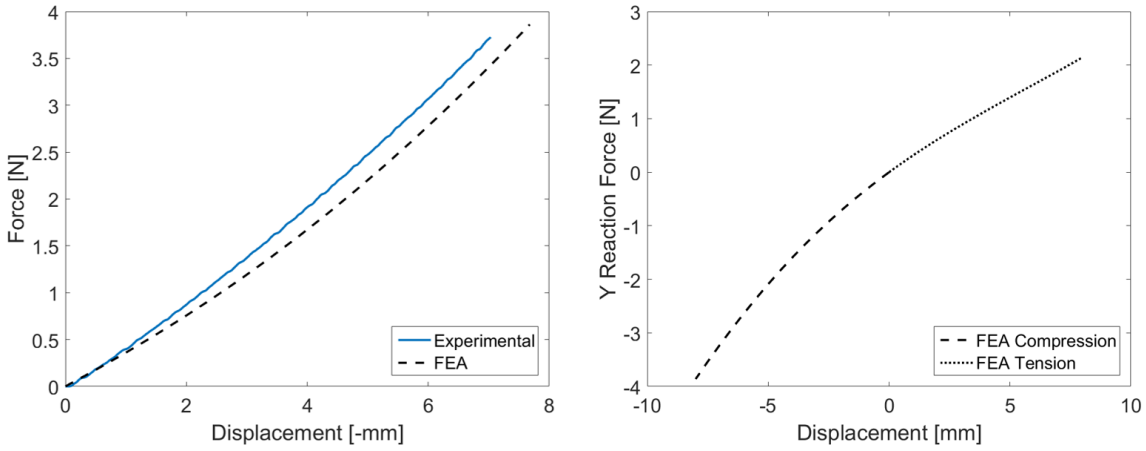

Figure 2.15: Left: Comparison of FEA and experimental data for the non-contact stiffening lattice. Force is measured at the load cell. Right: Same lattice simulated in compression and tension. Note that the Y reaction force is measured from the lattice side in the right graph; the blue curve on the right and the dotted black curve on the left are equivalent.

Both simulation and experimental data show that this particular version of the lattice have very minimal stiffening curves (Figure 2.15, left). However, the J-curve may be amplified by increasing the size of the unit cell and reducing increasing the ratio of the thick beam thickness to the thin beam thickness (Figure 2.16, $t = t_{thick}/t_{thin}$).

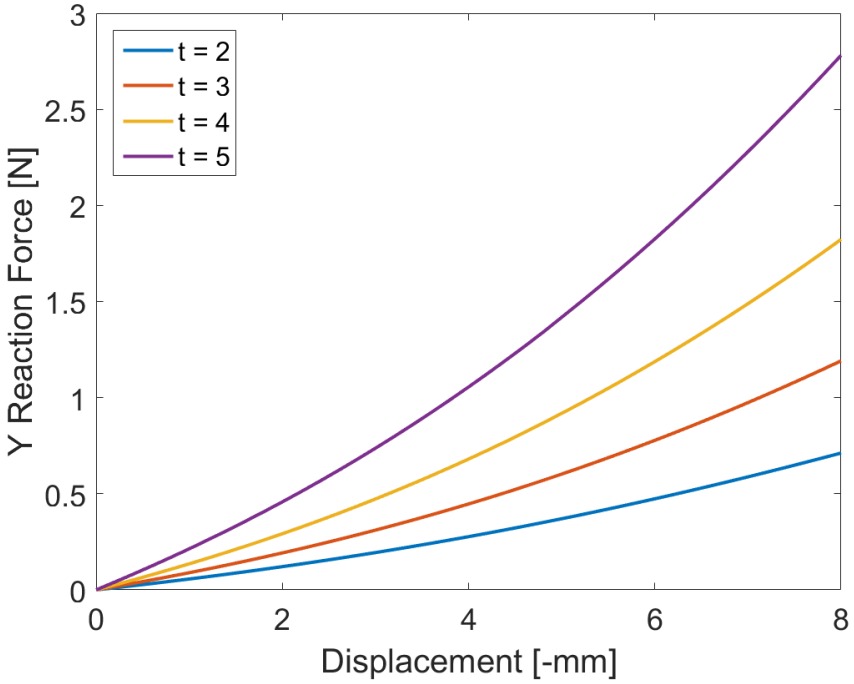

Figure 2.16: Simulated force-displacement curves for lattices of the same global dimensions but varying t values.

As the printed lattice only had a t of 1.5 due to printer constraints, a larger lattice with a higher t would likely display a more apparent stiffening behavior. Finally, the COMSOL model indicates that while this lattice stiffens in compression, it softens slightly in tension (Figure 2.15, right). This satisfies the "B" quadrant in the design domain in Figure 2.2.

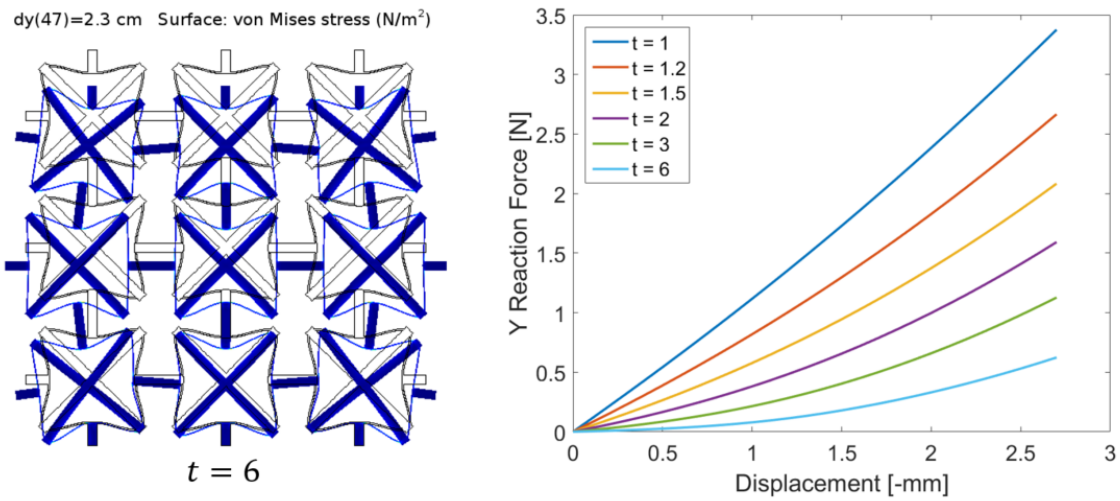

Figure 2.17: Left: 3 x 3 quadrilateral lattice undergoing compression in COMSOL simulation. Right: Simulated force-displacement curves for lattices of the same global dimensions but varying t values.

The quadrilateral lattice in Figure 2.17 was also shown to stiffen in compression, and to do so more dramatically at high t values, especially when compared to the hexagonal non-contact stiffening lattice. However, as discussed in the sections above, this lattice was prone to buckling due to the poor connectivity between the unit cells. This can be seen in the extreme rotations of the outermost unit cells in Figure 2.17, Left. For non-contact stiffening lattices of similar geometry, this indicates that a balance must be struck between connectivity (and thus stability of the structure) and tuning the stiffening J-curve: lattices of this type are constrained in their nonlinearity.

2.6 Conclusions

Three lattices were explored in FEA and experimentally. One softens under compression via tailored beam bending, while the other two stiffen under compression by contact or internal tension devices. While in all scenarios COMSOL simulations showed reasonable qualitative agreement with the experimental results, we expect the fit between experimental and

simulated data could be enhanced by a more sophisticated material model for TangoBlack. Lastly, despite multiple ideation sessions, a lattice that softens in both compression and tension could not be found. As shown in the softening lattice and the non-contact stiffening lattice, structures that rely on internal geometric nonlinearities to stiffen/soften under compression often soften/stiffen under tension. To achieve softening in compression and tension, we suggest that other nonlinearities such as buckling or activating material nonlinearity could potentially be employed.

Chapter 3
TOPOLOGY OPTIMIZATION

3.1 Objective

Heuristic exploration of the lattice design space helped develop intuition for the types of nonlinearities attainable through tailored lattice geometry. However, to study (i) the extremes of these nonlinearities and (ii) varying between these nonlinearities continuously, computational strategies are expected to be advantageous. Consequently, a topology optimization tool was developed to generate a structure to meet a prescribed load-displacement curve when compressed. The code structure for this tool is discussed in the following chapter.

3.2 Background

Topology optimization is a method for choosing material distribution within a design domain to create structures that satisfy an objective function. A common way to do this is the Simplified Isotropic Material with Penalisation (SIMP) method, which works to minimize compliance of a structure by strategically allocating a set amount of material (volume fraction) [24]. In SIMP, a domain is specified with static constraints and loading conditions. This domain is then subdivided, and each element in the space is given a "density" between 0 (no material, no stiffness) and 1 (full material, full stiffness) [24]. A structure that satisfies the domain constraints is created, FEA is performed on that structure, the structure's compliance is computed, the density of the material is redistributed by an algorithm of choice [24]. As mentioned above, minimization of compliance is also constrained by an initially set volume fraction: the optimizer must create the stiffest structure for a given amount of material in the design domain.

For example, Figure 3.1 below shows the design domain used for all optimization development described in this chapter. For visualization purposes, it has been subdivided into an 10 x 10 grid of elements, which which have densities of 0 (white) or 1 (black). The example structure in Figure 3.1 consequently satisfies a volume fraction of 0.5.

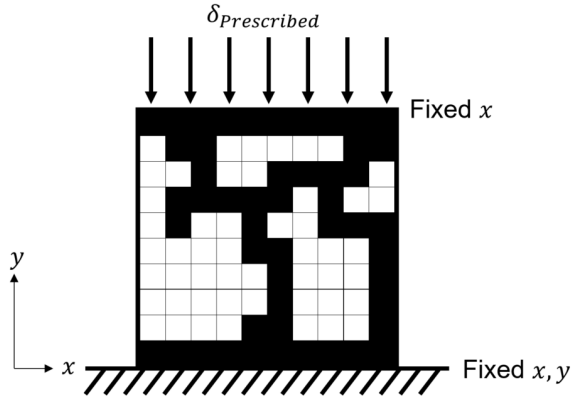

Figure 3.1: Example design domain and loading conditions used in the topology optimization discussed in Section 3.3 below.

For static loading conditions with the objective of reducing compliance, topology optimization can be an extremely fast way of computationally designing lightweight, strong structures. Andreassen *et al.* developed an 88 line MATLAB code that uses a modified SIMP method to determine the geometries for different loading conditions and different volume fractions [25]. Topology optimization schemes can also be used to design structures undergoing large deflections, as methods can now account for geometric nonlinearity [26] [27]. Furthermore, as topology optimization often generates organic, hard-to-machine structures, it has recently been integrated into additive manufacturing optimization tools as well [28].

3.3 Code Outline

To determine lattice structure that would have a nonlinear loading response, the optimizer must take into account geometric nonlinearity as well as ensure that the structural response follows a prescribed load-displacement curve. This objective function differs significantly from the minimal compliance sought by SIMP, and consequently required a new strategy. The preliminary framework for this code is described in this section.

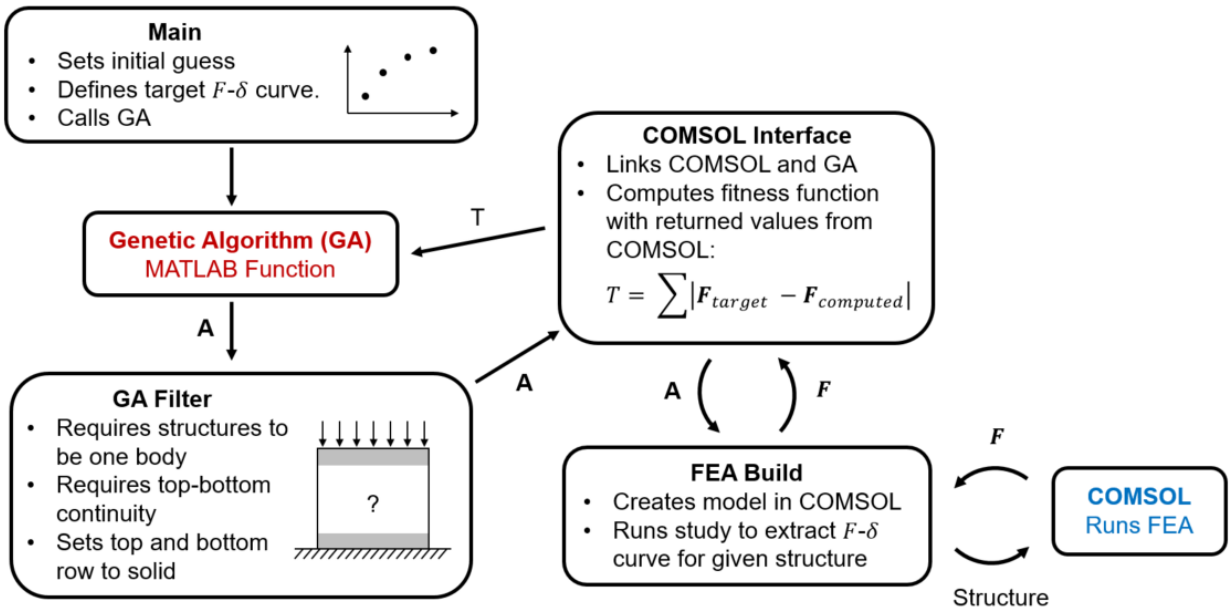

Figure 3.2: Flow chart for the topology optimization tool.

Figure 3.2 shows the framework for topology optimization code that generates nonlinear structures under the loading conditions seen in Figure 3.1. It makes use of the built-in MATLAB genetic algorithm (GA) functions as well as COMSOL LiveLink, which enables the optimizer to run FEA with geometric nonlinearity on the proposed structures. It is explained in detail below, while the code can be found in Appendix B.

Main In MATLAB, the optimization parameters are set in the **Main** file. Here, the user

sets the target force-displacement curve for the desired structure, defines the resolution on the domain as well as sets an initial guess for the structure. The default for this guess is a structure that is a solid block of material. Settings such as tolerances, timeout limits and plotting outputs for the genetic algorithm are also set in this file (Table 3.1). Finally, when this file is run, it calls the **Genetic Algorithm** function.

Genetic Algorithm Genetic algorithms select a random population of solutions, and evolves these solutions iteratively toward convergence, creating the next generation of solutions by mixing the most "fit" solutions from the current population [29]. Consequently, the genetic algorithm was selected as the optimization algorithm for its ability to meet nonlinear objective functions [29], handle optimization of discrete problems, and easily escape local minima unlike gradient-descent methods. Like in SIMP or other topology optimization strategies, the design domain is subdivided in this method and each element is considered a variable for the genetic algorithm. However, to speed up iterations, densities are either one or zero; this binary settings differs from the gradient often used by SIMP.

GA Filter When the genetic algorithm creates a potential solution, it sends it to the **GA Filter** function in the form of the **A** matrix, a full matrix the same size as the domain with ones and zeros representing the presence or absence of material. The purpose of this function is to prevent COMSOL from failing when it performs FEA on the structure. **GA Filter** checks that the proposed structure:

- Is one body (i.e. there are no floating regions of material).
- Is a contiguous structure from top to bottom. This permits compression forces to be transmitted from top to bottom of the structure.
- Has a completely solid top and bottom row. This allows the prescribed displace-

ment to be applied consistently to structures, as well as enables easy computation of reaction force along the bottom of the structure.

Should the proposed structure fail these constraints, the **A** matrix is given a poor fitness value in genetic algorithm and it does not move onto the FEA stage. Instead, the genetic algorithm creates a new possible solution—a new **A** matrix—and tries again.

COMSOL Interface When the **A** matrix clears the GA filter, it passes to **COMSOL Interface**, a function that links the **FEA Build** function with the genetic algorithm code. When passed reaction force vector ($\boldsymbol{f}$) upon FEA evaluation by COMSOL, **COMSOL Interface** also computes the fitness (objective) function. The fitness function evaluates the sum of the differences between the target force value (F) and the computed force value (f) at N displacements.

$$T = \sum_{n=1}^{N} |F_n - f_n| \tag{3.1}$$

The fitness value, scalar T, is passed back to the genetic algorithm as a description of the current solution. The genetic algorithm will attempt to minimize T.

FEA Build The **A** matrix is next passed to the function **FEA Build**, which uses LiveLink commands to build an appropriate COMSOL model to perform FEA on the structure. LiveLink is a Java API that enables creation, manipulation, and data analysis of COMSOL models from the MATLAB environment [30]. A for-loop checks each element in the **A** matrix and places a block of material for each element denoted by 'one' to create the proposed structure (scaled to be 1 x 1 meters). Next, the top and bottom boundaries of the structure are selected and the prescribed displacement and fixed constraint are applied, respectively. Finally, **FEA Build** requests COMSOL return the Y reac-

tion forces computed along the bottom of the structure at each prescribed displacement step to form the $\boldsymbol{f}$ vector.

COMSOL Finally, COMSOL runs the parametric study set up in **FEA Build**, where each step in the study is an incrementally increased compressive displacement applied to the structure (Figure 3.1). The material properties used are those of TangoBlack ($E = 6.95$ x 10^5 Pa, $\nu = 0.4$), and the 2D simulation is in plane strain, with a depth set to 1 m. Each model is meshed by triangular elements on the default mesh size setting. Most importantly, the structures are modeled *using the geometric nonlinearity option.* All of these options can be set in **FEA Build**; current settings enable COMSOL to perform analysis of a single build in ≈1 second.

.

The MATLAB/LiveLink code described in this section and used to generate the results discussed below can be seen in Appendix B.

3.4 Optimization Results

To validate this topology optimization code, a force-displacement curve for an I-beam was generated in COMSOL (Figure 3.3, top right). This structure fit within the 1 x 1 m design domain of the genetic algorithm and was compressed by 2 cm (-0.02 strain) in 10 steps; this small deformation was chosen to guarantee convergence for a wide range of geometries in COMSOL. With the design domain subdivided into a 10 x 10 space, the genetic algorithm was called using the settings in Table 3.1. Further description of genetic algorithm settings can be found in online MATLAB documentation for "ga" [31].

Table 3.1: Genetic Algorithm Settings

Option	**Value**	**Comment**
FitnessLimit	100	Halts optimization once T drops below this value.
TimeLimit	6 x 10^8	Prevents simulation from timing out early.
InitialPopulation	$\boldsymbol{A_{initial}}$	Sets initial guess to solid block.
StallTimeLimit	6 x 10^8	Prevents simulation from timing out early.
TolFun	0.1	Relative tolerance; ends computation when met.
StallGenLimit	25	Number of generations TolFun is computed over.
PopulationSize	50	Size of initial population.
Generations	50	Max number of generations.

With force-displacement input from the I-beam as the target $\boldsymbol{F}$, the genetic algorithm generated an alternate geometry (Figure 3.3, bottom right) with a comparable force-displacement curve (Figure 3.3, left).

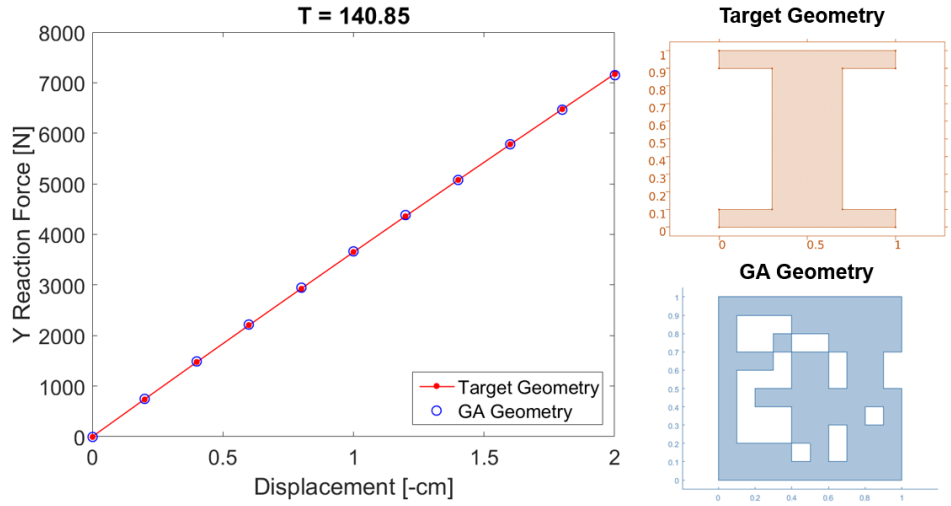

Figure 3.3: Finding a structure to match a load-displacement curve. Upper right: Target geometry (I-beam) used to create target force-displacment curve. Lower right: GA-generated geometry that provides a similar load-displacement curve. Left: Comparison of their load-displacement curves.

The difference in shape between the two structures can be attributed to the fitness function (Equation 3.1) not penalizing the optimizer for excess mass as SIMP does as well as the existence of many other solutions.

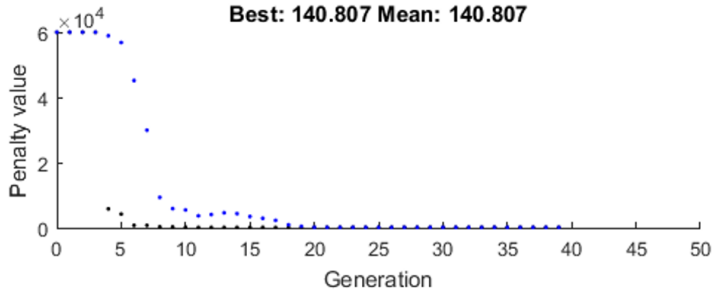

Figure 3.4: Convergence to the solution shown in Figure 3.3. Blue dots: Mean T value across the population. Black dots: Best T value in the population.

Convergence to the solution is shown in Figure 3.4.[1] The optimization process terminated at 39 generations when the TolFun conditions was met, i.e. when the deviation from T over the prior 25 generations was less than 0.1. Convergence on a Dell XPS 8900 workstation with 16 GB RAM took $\approx$ 48 minutes.

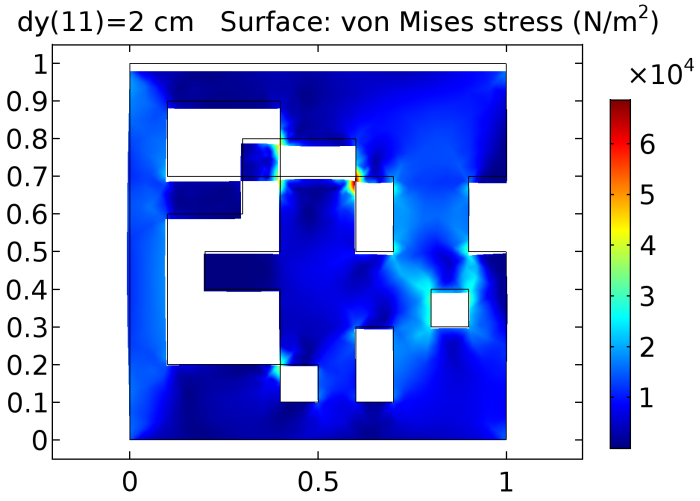

Figure 3.5: Von Mises stress in the structure developed by the genetic algorithm.

Figure 3.5 shows the geometry generated by the genetic algorithm at 2 cm of displacement. This illustrates that the GA structure is stable when simulated.

3.5 Errors and Next Steps

To reduce the the multitude of solutions available to the genetic algorithm, a thin I-beam was simulated and its force-displacement curve was used as the target $\boldsymbol{F}$.

[1]What MATLAB refers to as the "penalty value" is referred to as the "fitness value" or T in this work.

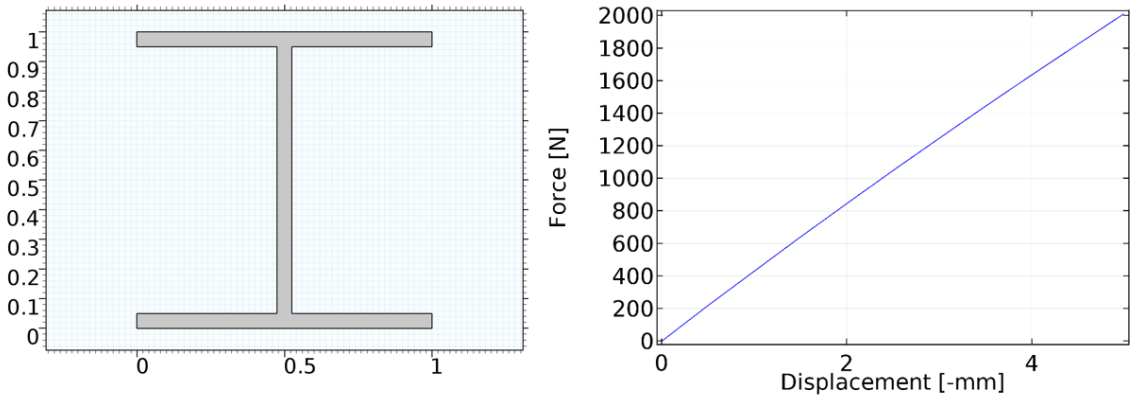

Figure 3.6: Left: Thin I-beam geometry. Right: Force-displacement curve the I-beam under compression.

As the design domain was subdivided into 10 x 10 elements, the I-beam was sized to be exactly one element wide (Figure 3.6) to force the optimizer to develop some variation on this geometry.

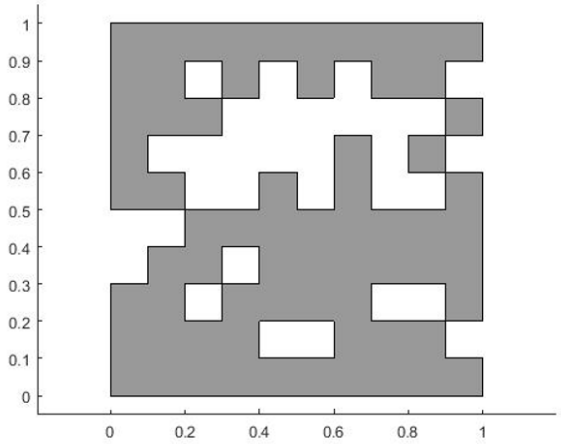

Figure 3.7: Geometry generated by the genetic algorithm to match the thin I-beam geometry.

However, the structure produced (Figure 3.7) crashed COMSOL in the 18th generation

(Figure 3.8). This geometry was poorly constrained due to its corner connections and the extra degrees of freedom caused the COMSOL solver to fail, killing the entire optimization run.

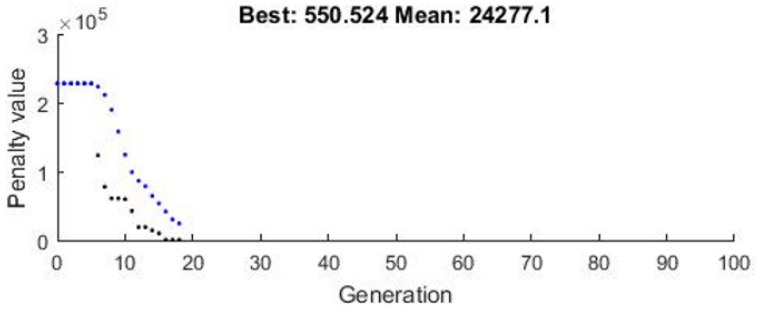

Figure 3.8: Convergence plot for the geometry in Figure 3.7.

It was observed during optimization that the genetic algorithm found this poorly connected structure in a local minimum, and was unable to escape by creating significantly different children between generations. Consequently, this topology optimization strategy could be refined with the following improvements:

- Improving the **GA Filter** to prevent poorly connected structures like the one in Figure 3.7 reaching COMSOL. The new filter should require each element of material to have at least one neighbor that shares a side with it to prevent corner-connected structures.

- Adjusting GA settings for a higher population size and more diverse mutations to further prevent the optimizer sticking in local minima.

- Parallelizing the nonlinear FEA (COMSOL) function in order to reduce computation time.

3.6 Conclusions

A topology optimization method using a MATLAB genetic algorithm and COMSOL FEA (with geometric nonlinearity) was developed to find structures to match prescribed load-displacement curves. It is shown to work for small displacements (Figure 3.3), but sometimes can produce poorly connected structures (Figure 3.7) that cause the failure of the finite element simulation. Should its filter function be improved and the genetic algorithm options better tailored to this process, local minima could likely be avoided and convergence to useful, stable structures encouraged. With these improvements implemented, this approach could be applied to generating nonlinear lattice geometries by introducing periodic boundary conditions and attempting to solve for nonlinear force-displacement curves.

Chapter 4

QUASI-STATIC CHARACTERIZATION OF SPIROPYRAN IN PDMS

4.1 Objective

In order to explore how microstructure affects mechanophore activation, characterization of the mechanophore crosslinked polymer of choice (spiropyran crosslinked with PDMS) was first required. Quasi-static (discussed in this section) and dynamic tests were planned to understand (i) what strain is required to activate spiropyran in our selected medium, (ii) how fast this activation occurs, and (iii) how this activation appears in real time. The following quasi-static tests were intended to address the first of these questions as well as clearly visualize how spiropyran activates in high-strain regions.

4.2 Literature Overview

Mechanophores are molecules that activate under mechanical force, and spiropyran, a color-changing mechanophore, was chosen to explore the interaction of microstructure and mechanochemistry. When subjected to extreme strain, spiropyran opens into another isomer that is purple or blue and returns to its closed, largely colorless form when exposed to white light [6].

Spiropyran has previously been embedded and studied in PMMA, where Kingsbury *et al.* applied torsion to PMMA samples and observed spiropyran activation via shear [32] and Hemmer *et al.* used a Split-Hopkinson Bar to compress PMMA at strain rates as high as 10^4 s^{-1} and then examine spiropyran activation in the resulting fractured pieces [8]. Furthermore, Kim *et al.* observed the change of spiropyran fluorescence *in situ* on compression and tension samples loaded quasi-statically [33]. Gossweiler *et al.* studied spiropyran embedded in thin

films of PDMS in tension, noting repeated activation of spiropyran can occur through the highly elastic material properties of PDMS [7]. Spiropyran has also been embedded in polycaprolactone (PCL), which Peterson *et al.* then 3D printed via the fused deposition method, showing that mechanoactive polymers may be shaped via additive manufacturing [9]. A widely studied mechanophore, spiropyran has primarily been characterized in tension and compression in polymers that experience extreme plastic deformation or fracture at the strains necessary to achieve activation.

4.3 Quasi-Static Test Setup

4.3.1 Sample Preparation

Since tests were to be conducted at low- and high strain rates, studying spiropyran necessitated a highly deformable, elastic bulk material into which spiropyran could be cross-linked. Consequently, polydimethylsiloxane (PDMS) was chosen: a viscoelastic silicone that can withstand extreme compressive strains, PDMS enabled repeated experimentation in both quasi-static and dynamic tests. Using PDMS represented a departure from many previous studies ([8], [33]) that report on the behavior of spiropyran in highly brittle PMMA (acrylic), and thus validating our sample fabrication procedure through material characterization was essential to our project.

PDMS was further chosen as its cross-linking, and thus it stiffness, can be easily controlled by varying the base:curing agent ratio. The PDMS used in these experiments, Dow-Corning's Sylgard 184, comes in two parts for easy storage that cure into a solid viscoelastic material when mixed. Wang reports that an inverse exponential relationship between elastic modulus (E, MPa) and base:curing ratio (n) for Sylgard 184 PDMS [34].

Selection of the stiffness of samples was based on previous experimentation within the Boechler group, which indicated that a base:mixing ratio of 10:1 or softer was required to reach $>$0.7 strain on the lab spring-loaded drop tower (discussed in Chapter 5), as well as

provide sufficient cross-linking in order to activate spiropyran. Consequently, multiple 25 x 25 x 35 mm samples with and without spiropyran were fabricated out of 15:1 PDMS. This process involved mixing the base, curing agent, and spiropyran, placing the mixture in a vacuum to remove it of bubbles, and then curing the mixture in square molds overnight in an oven (discussed in further detail in Appendix A).

Figure 4.1 shows a mold filled with PDMS that has been put under vacuum repeatedly to remove all bubbles introduced via the mixing process. It was observed through initial compression testing that impurities and cavities in the samples created stress concentrators in the samples, causing them to fracture prematurely, so preventing their inclusion became an essential part of sample preparation.

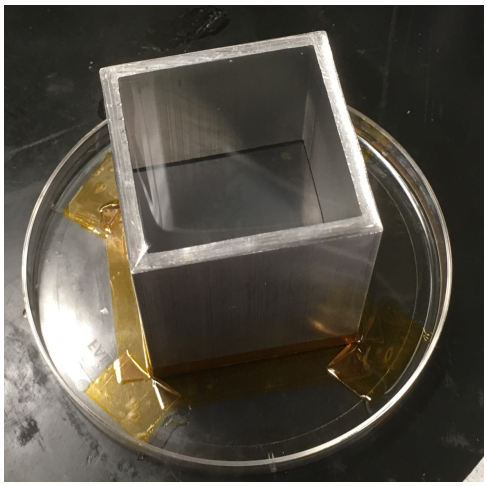

Figure 4.1: Liquid PDMS curing in its aluminum mold.

Following the curing process, the samples were removed from the molds and tested in the setup shown in the following section.

4.3.2 Compression Testing

Quasi-static compression testing was conducted on an Instron 5585H load frame using a 10 kN load cell recording displacement and load. Compression occurred at 50 mm/min and load and crosshead displacement were recorded. As the activation of spiropyran is indicated by a color change from light gold-brown to deep purple under compression, activation was captured visually via a Nikon D5600 recording at 30fps in 1080p resolution (Figure 4.2) against a white background.

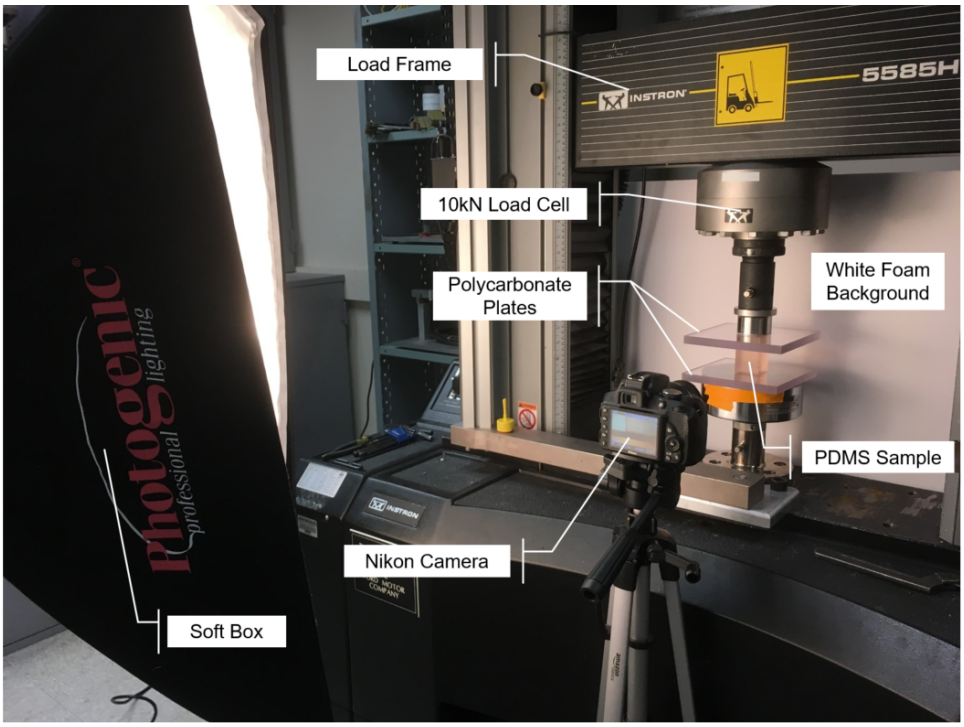

Figure 4.2: Test setup for quasi-static testing, complete with softbox (left).

Initial compression tests using conventional metal platens cast a shadow on the samples, making it difficult to visually detect when the sample changed color due to spiropyran activation. To combat this, the sample was compressed between two clear 0.5" thick polycarbonate plates (Figure 4.3) and illuminated using a photography softbox (Figure 4.2).

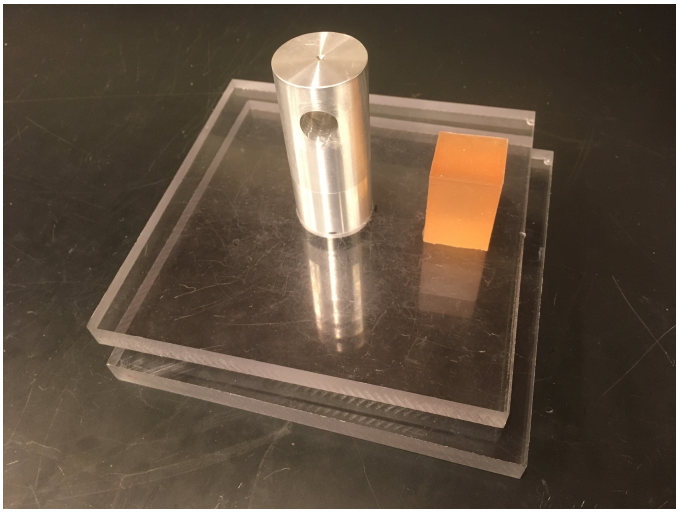

Figure 4.3: Test fixtures created for compressing testing, shown with a spiropyran-PDMS test sample for scale. The metal component is compatible with Instron fixturing, and fits into a circular pocket milled into the polycarbonate plate to prevent side-side movement of the plate during loading.

The diffuse light provided by the softbox provided a well-lit filming environment without resetting the spiropyran.

4.4 Quasi-Static Activation

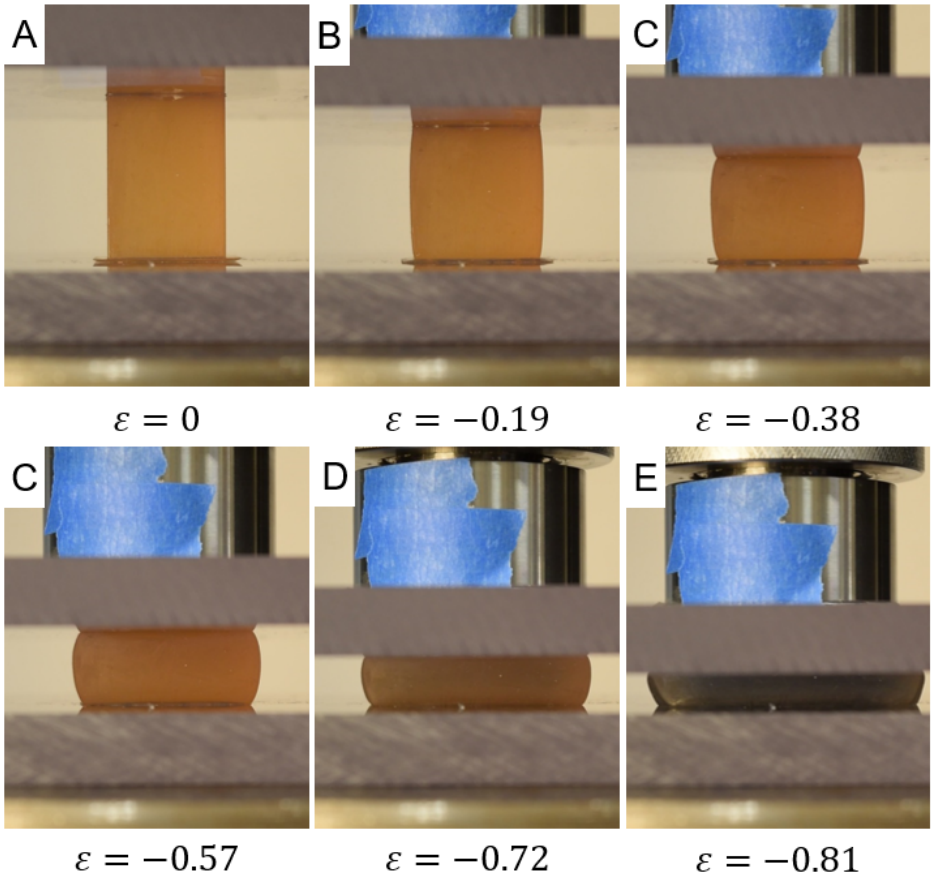

Figure 4.4: Frames from the compression test video. In (D), the start of spiropyran activation can be seen, while (E) shows the entire sample changing color due to the extreme strains.

As shown in Figure 4.4, the spiropyran-PDMS sample was highly compressed over the course of the quasi-static test. At about 0.7 compressive strain, the initial spiropyran activation can be seen in the center of the sample. Over the next 0.1 compressive strain, the color change radiates from the center of the sample to its edges until the entire sample changes color to a deep purple at roughly the same speed of loading.

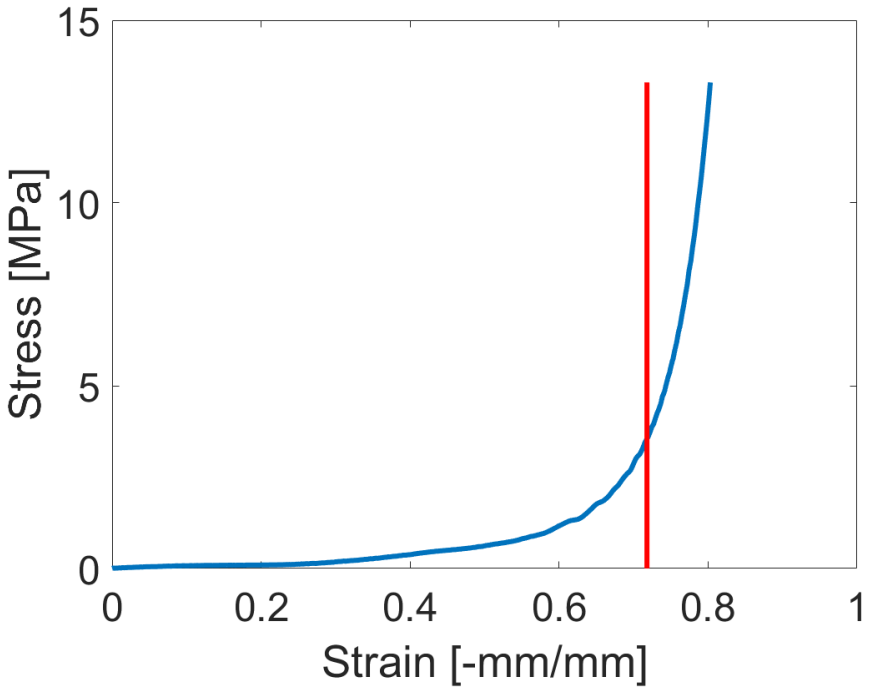

Figure 4.5: Stress-strain plot for the spiropyran-PDMS sample. Estimated onset of activation is indicated by the red line at -0.72 strain.

As seen on the stress-strain plot in Figure 4.5 above, the sample begins stiffening exponentially around -0.5 strain. Regardless of the extreme compression the sample is subjected to, the sample returns to its original shape and dimensions once unloaded (Figure 4.6).

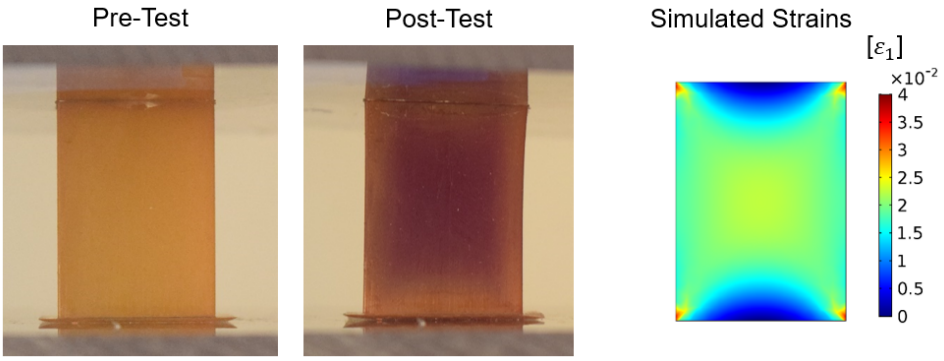

Figure 4.6: Pre- (left) and post-compression (middle) PDMS samples. The first principal strains in a a comparable block compressed 20% in COMSOL (right).

The post-test image in Figure 4.6 illustrates the vibrant color change undergone by the spiropyran molecule within the PDMS sample as well as indicates that the highest strains are found within the center of the sample. This strain pattern matches the one found via a simulation of a cube compressed (Figure 4.6) in COMSOL, confirming that spiropyran is indeed activating the most in areas where the first principal strain is greatest.

4.5 Conclusions

Through this quasi-static compression test, the activation of spiropyran in 15:1 PDMS is found to occur at about 0.7 strain. Simulated first principal strains—the greatest local strains—match well with the visual pattern of spiropyran activation found in post-test samples. These findings indicate that in quasi-static compression, spiropyran in 15:1 PDMS will activate in areas where local strains exceed 0.7.

Chapter 5

DYNAMIC CHARACTERIZATION OF SPIROPYRAN IN PDMS

5.1 Objective

As mentioned in Section 4.2, spiropyran had been studied at high strain rates post-impact via Split-Hopkinson Bar [8], and shown to activate at lower (7%) strains in thin films experiencing shockwave loading [35]. Consequently, the objective of the tests described in this section are to visualize spiropyran activation *during* a dynamic compression test as well as to determine how fast the activation reaction occurs. These tests aim to answer the question: **how fast does mechanophore activation occur?**

5.2 Dynamic Test Setup

Dynamic tests were performed using the spring-loaded drop tower shown in Figure 5.1. With a lightweight aluminum striker, this custom impact tester may reach high speeds at relatively low kinetic energies, to strain but not destroy the comparatively soft PDMS samples. In this device, the striker plate is accelerated to a maximum of 11.5 m/s via springs that are compressed with the winch at the top of the structure. The test is initiated by manually pulling a quick-release latch. For these dynamic tests, the pulse-shaping stoppers at the bottom of the drop tower were removed and the same 25 x 25 x 35 mm PDMS samples created for quasi-static tests were subjected to uninhibited compression by the striker.

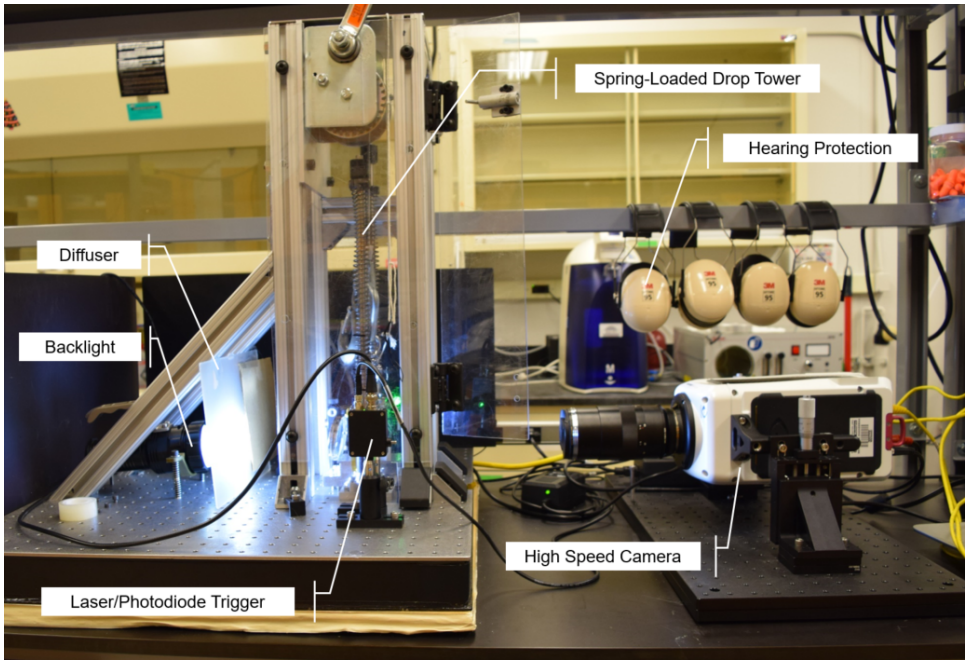

Figure 5.1: Test setup for dynamic testing.

Figure 5.1 also shows the data acquisition setup for the dynamic tests discussed in the following sections. Grayscale high speed videos were captured at frame rates up to 20,000 fps using a Phantom v711 (Figure 5.1, right) with a Zeiss macro lens, while color videos were captured at 60 fps using a Nikon D5600 (not shown). High speed camera triggering was provided by a laser interrupt system (center of Figure 5.1, green laser on and visible), in which the striker passes between a Thorlabs CP532-C2 laser and receiving Thorlabs PDA10A photodiode just prior to impacting the sample. The change in voltage output from the photodiode generates a square wave from a signal generator (not shown) to the high speed camera, starting the recording process. The output of the photodiode was also measured using an oscilloscope (not shown), from which the speed of the striker was ascertained.

As spiropyran activation was evaluated using visual techniques, lighting the sample well was essential in quasi-static (Section 4.3) and especially dynamic tests. Samples were back-

lit with a bright flashlight[1] from behind a translucent plastic diffuser. Furthermore, to specifically illuminate the sample and not saturate the sensor in the high speed camera, the diffuser was partially covered with cardboard until only a slit permitted the bright white light through (best seen in Figure 5.2). Tests on spiropyran-PDMS and control PDMS samples were conducted using this setup.

5.3 Dynamic Activation

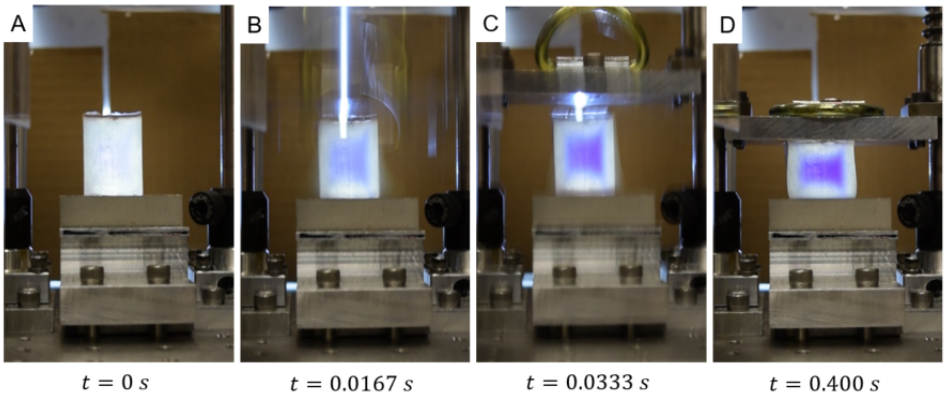

Figure 5.2: Frame-by-frame color images from the video of the the sample undergoing impact. A) Frame immediately prior to impact. B) Frame immediately post impact, 0.0167 seconds later. Activation is visible. C) Frame following (B), showing the striker bouncing off the PDMS sample. D) Activation after the impact tester and sample have reached equilibrium.

Figure 5.2 above shows a sample before and after impact, illustrating the vibrant purple resulting from activated spiropyran. Again, the activation is localized in the center of the sample experiencing the most strain, with small tails reaching from the center to the corners of the rectangular sample (which are stress/strain concentrators). When compared to the quasi-static activation pattern seen in Figure 4.6, it is clear that the activation pattern is solely dependent on high strain areas irrespective of strain rate.

[1]It should be noted that light sources using AC power (without a DC converter) could not be employed in these tests as they flash at frequencies detectable by the high speed camera.

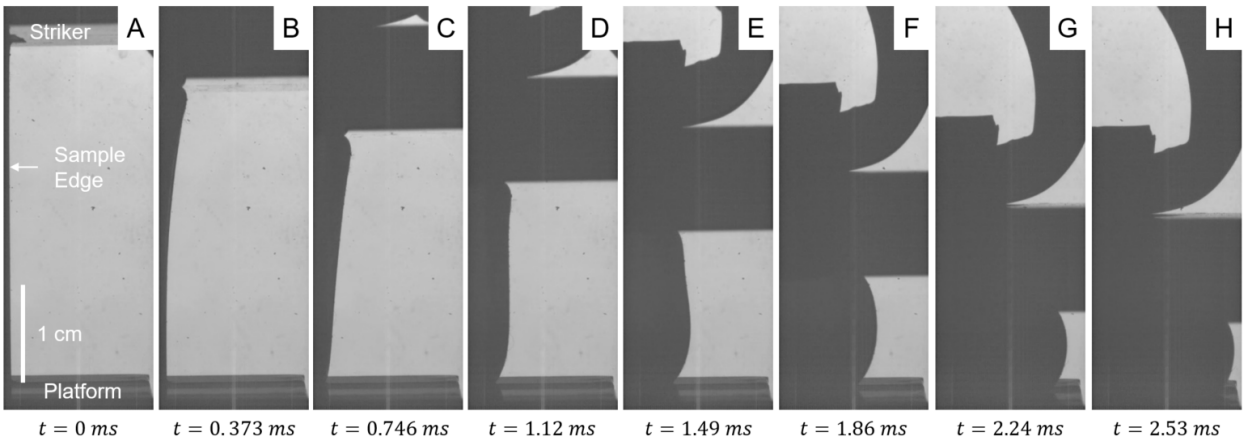

Figure 5.3: Deformation of the edge of the sample captured with the high speed camera at 26,000 fps. Frame H shows the PDMS sample at maximum deformation.

Deformation of the edge of the sample is shown in Figure 5.3. The sample is compressed 80% in 2.53 ms (strain rate of 320 s^{-1}), and as the striker is not stopped after impacting the sample, no impulse is seen in the edge deformation of the PDMS.

5.3.1 Activation Speed

To estimate the time required for activation, the high speed camera was focused at the center of the sample instead of the edge. The images in Figure 5.4 were captured at 13,662 fps and an exposure of 70 μs, which was sufficiently high capture the color contrast generated by the activated spiropyran but not saturate the camera.

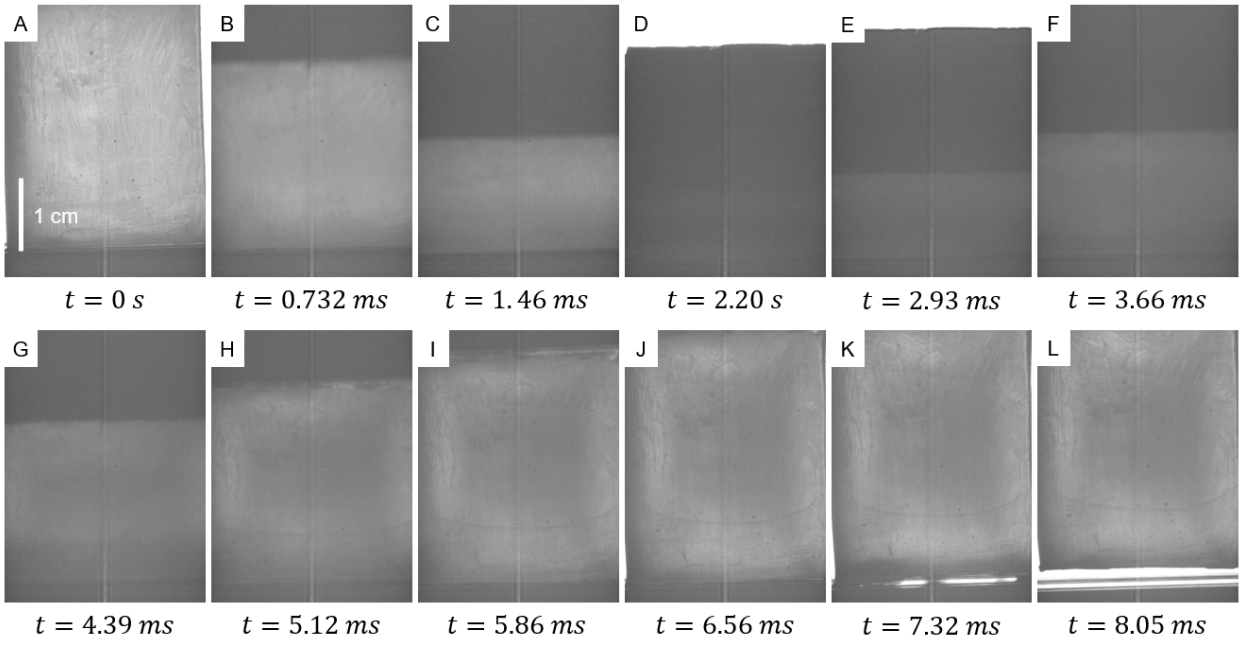

Figure 5.4: Frames from the center of the compressed sample. Compression occurs in frames A-D and activate spiropyran is visible upon striker release, frames E-L. Also captured is the sample bouncing off the platform in frames K, L.

For the 25 x 25 x 35 mm samples, the initial compression and release of the striker occurs within 8 ms. Due to the sample bulging out at high compressive strains, the deformed sample forms a lens through which the backlight is obfuscated and the camera cannot resolve the spiropyran activating. As a result, it is difficult to determine when the spiropyran begins to activate, although from Figure 5.4 it is apparent from that activation is visible upon striker release (Figure 5.4 G-H).

5.3.2 Wave Investigation

In the high speed video used to generate Figure 5.4, a small "ripple" was observed travelling from top to the bottom of the sample upon impact. To to determine if this ripple was a wave of spiropyran activating through the sample or simply a side affect of the material deforming,

the dynamic tests were repeated on control and spiropyran-PDMS samples. Control samples of 15:1 PDMS were fabricated without spiropyran but contained the same amount of xylenes to achieve a similar stiffness to the spiropyran-embedded samples.

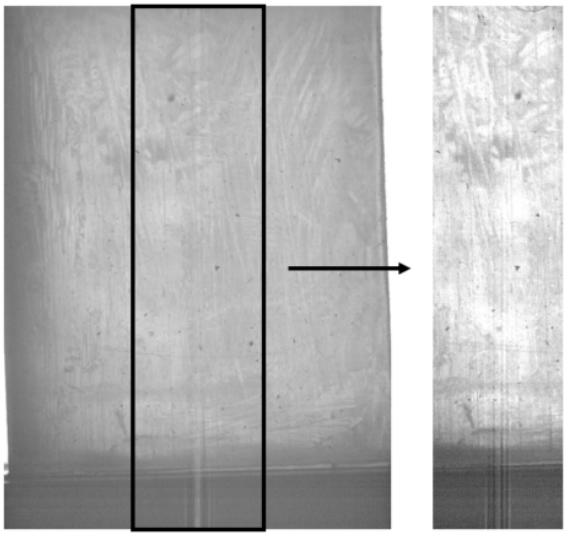

Figure 5.5: The previous activation speed experiment (left) and the new framing of the wave investigation (right).

For better imaging of the wave, the frame rate of the high speed camera was increased from 13,662 fps to 20,000 fps, and to maintain video resolution at this new frame rate, the frame size was reduced to the center of the sample as shown in Figure 5.5. For the spiropyran-PDMS samples, the exposure was still set at 46 μs, while the control PDMS was captured at an exposure of 10 μs to once again protect the camera sensor from saturating.

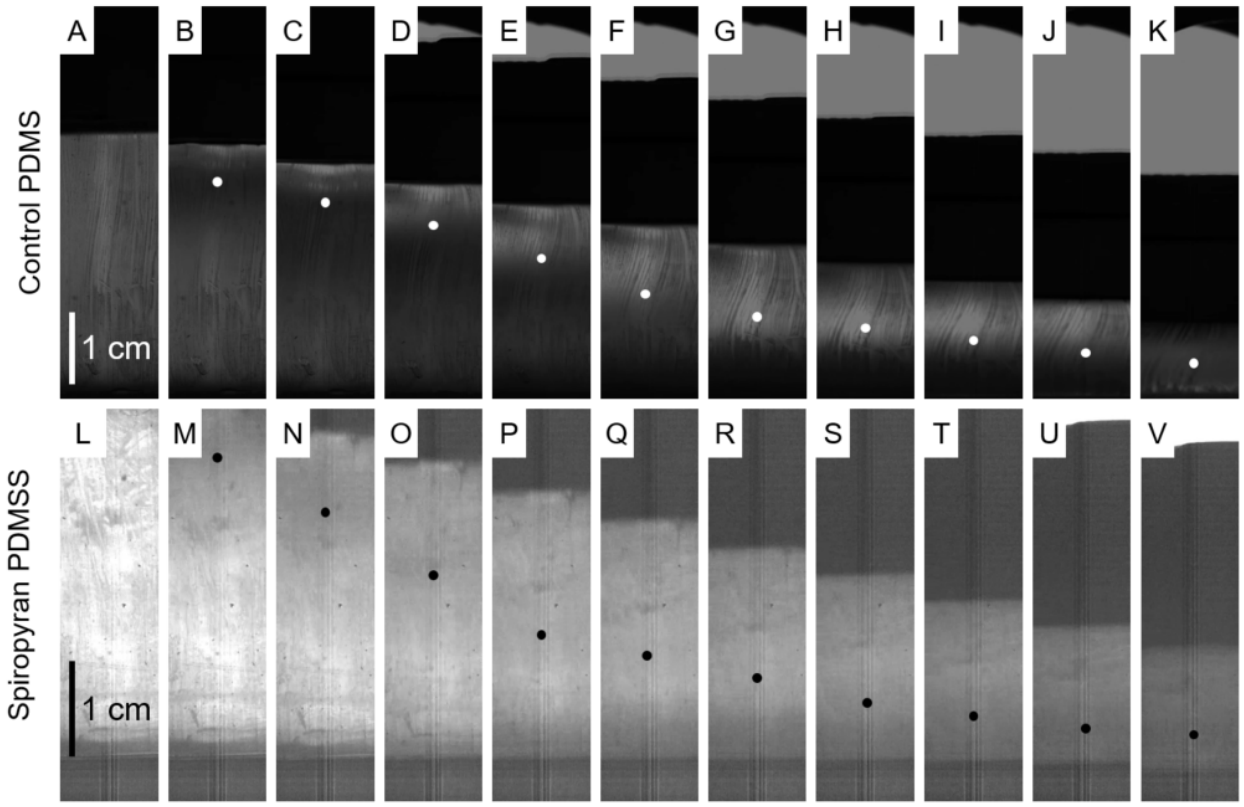

Figure 5.6: Comparison of the control to the spiropyran-PDMS; images are 0.200 ms apart. Contrast in the spiropyran-PDMS images have been enhanced in Adobe Premiere Pro. Both image sequences are initiated at contact between the sample and striker and dot markers indicate approximate location of each "wave" (determined visually).

Figure 5.6 shows the "ripple" seen in the original activation tests, which appears as a dark section travelling down the spiropyran-PDMS samples (L-V). However, this wave also appears very clearly in the control sample (Figure 5.6) and is likely connected to local material deformation. Furthermore, this experiment suggests that even if there was a wave of spiropyran activation within the material, it would be masked by the material curving. This suggests that future tests might have to detect dynamic spiropyran activation in real time using alternative methods.

5.3.3 Large Drop Tower Experiment

In addition to the experiments on the spring-loaded drop tower, a spiropyran-PDMS sample was also compressed using a Instron Dynatup 9250HV impact tester and its impact recorded with the Nikon D5600 camera at 60 fps.

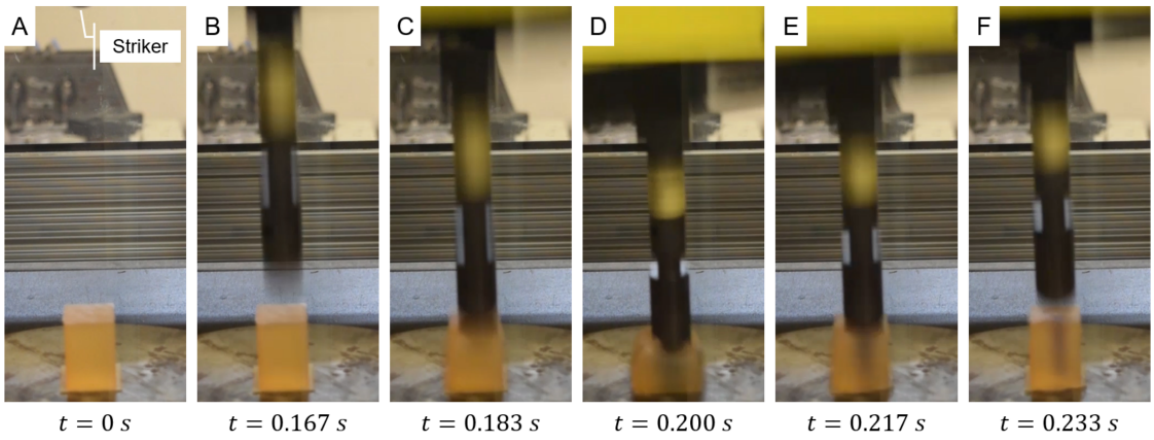

Figure 5.7: Frames from the large drop tower experiment. Frames B-F are successive frames captures at 60 fps; frame D shows first activation.

The 20 mm diameter ball-end striker, weighing 7.56 kg, was dropped from a height of 0.15 meters onto the sample (Figure 5.7). This drop input 11.1 J of energy into the sample, and the striker was measured moving at 1.7 m/s upon impact. This experiment illustrated that activation can occur at medium strain rates and at a higher energy (11.1 J, compared to 8.84 J provided by the spring-loaded drop tower [estimated by $\frac{1}{2}mv^2$]). Activation in Figure 5.7 is also seen in a small column of material directly below the radius of the ball end striker.

5.4 Conclusions

From these dynamic experiments, it was determined that activation occurs within the striker release time ($<$ 8 ms) and that activation becomes visible upon retraction of the striker at 80% compressive deformation. This suggests for this strain rate (320 s^{-1}), the activation

strain does not significantly reduce from the quasi-static value of 0.7 strain (measured at a strain rate of 0.024 s^{-1}). However, there was substantial difficulty in capturing real time spiropyran activation inside the highly strained samples due to the camera losing focus on the surface of the sample as well as the backlight being unable to penetrate the samples in their barreled state. A potential wave was identified as passing through the spiropyran samples, but comparison to control samples indicates that this was likely a result of the material distorting under impact and that any activation would be indistinguishable from the material deformation. Finally, local activation of spiropyran was seen in a medium strain rate impact test using a ball end striker, showing a sharp contrast between areas critically strained to activation and those were not. This test suggests that activation is not a gradient approaching 0.7 strain; activation only occurs strictly after 0.7 strain is reached.

5.5 Future Steps

There are several extensions and/or improvements that could be made to this project, which are listed below:

- As optically identifying the speed of spiropyran activation was difficult due to sample deformation, repeating these tests with a fluorimeter to measure spiropyran fluorescence would provide quantitative, real-time data [33].

- In order to better induce a wave of activation in the sample, a large local strain must be inputted into the sample. The striker moving at 11.5 m/s was likely not moving fast enough to create an impulse of significant strain (with pulse width smaller than the sample length) to cause a wave of activation to transmit through the sample. Using a Split-Hopkinson Bar is likely a better option to further this study.

- In some poorly-made samples, the PDMS fractured around stress concentrations like impurities or cracks in the bulk material. Imaging a high-speed fracture test may reduce

the problems due to sample deformation in compression and still while still providing a visible wave.

Chapter 6

SPIROPYRAN ACTIVATION IN LATTICE MATERIALS

6.1 Motivation and Introduction

Many lattice structures can be found in nature such as in bone or cell walls. Not only do these formations provide structure, they interact chemically with their surroundings [12]. Lattices embedded with mechanophores can similarly respond chemically to loading. Consequently, this section explores how to amplify spiropyran activation using lattice architecture, and seeks to answer the question: **how can microstructural lattice geometry enhance mechanophore activation?**

Choosing what lattice structures to use was determined by simulation of a bend-dominated, statically-determinate, and stretch-dominated lattice each. These were, respectively, the diamond, Kagome, and triangle lattices shown in Figure 6.1.

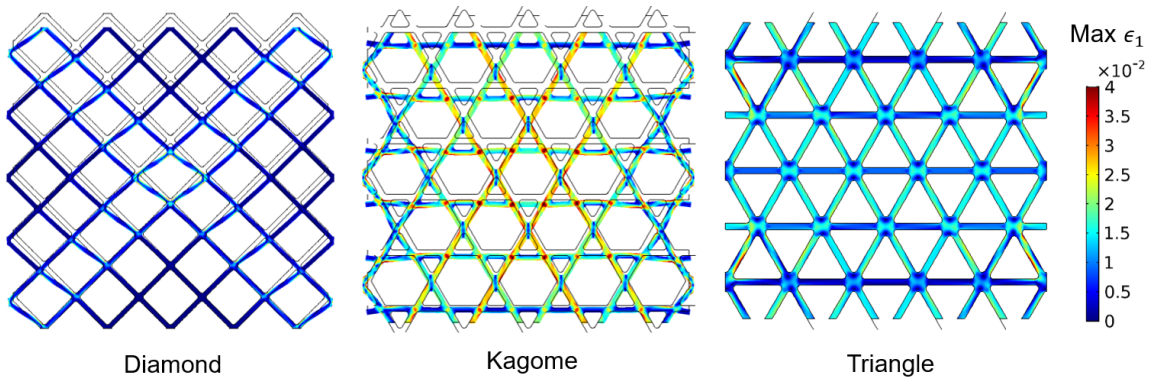

Figure 6.1: Comparison of first principal strains ε_1 (ϵ_1) within a diamond, Kagome, and triangular lattice.

Due to its bend-dominated nature, the diamond lattice responds to compression with

bending at the nodes. Deformation and consequently principal strains are localized to the center unit cell. In contrast, the stretch-dominated triangle and Kagome lattices have a fairly uniform distribution of strain, ensuring that any strain-activated mechanophore would have even activation throughout the lattice.

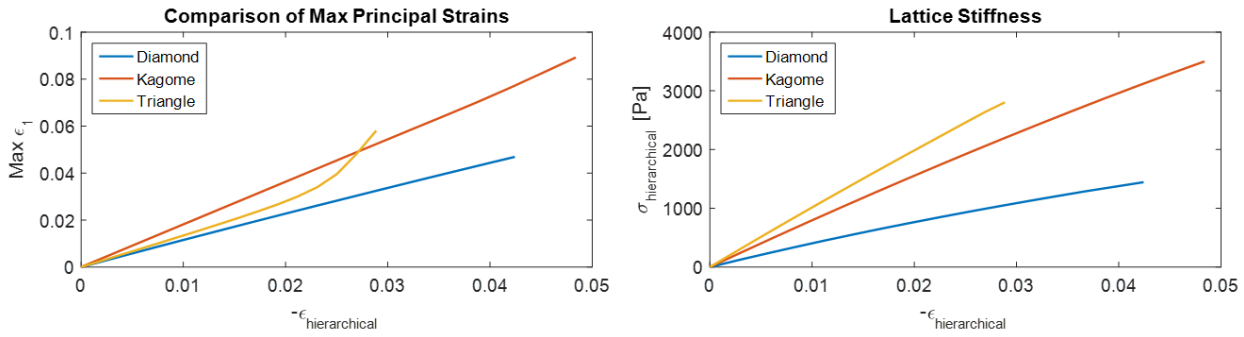

Figure 6.2: Left: Comparison of max principal strain vs. global ("hierarchical") strain. The uptick in the triangle lattice curve is due to the structure buckling. Right: Comparison of global stress vs. global strain.

Figure 6.2 shows that the Kagome lattice amplifies the global strain applied to it by about 2x in this configuration, exceeding the amplification effects of the triangle and diamond lattices. However, unlike the over-constrained triangular lattice, the Kagome lattice does not buckle under small strains while being nearly as stiff (Figure 6.2). Consequently, the Kagome lattice was the first lattice to be studied in conjunction with mechanophore activation.

6.2 PDMS Kagome Lattice

A Kagome lattice was fabricated out of 10:1 PDMS containing the equivalent percentage of spiropyran as one of the quasi-static/dynamic blocks described in Chapters 5 and 6. It was produced by printing a negative mold from polyvinyl alcohol (PVA), pouring and curing the PDMS into this mold, and then dissolving away the PVA via a hot water bath. It was then compressed in the Instron at 20 mm/min according to the setup in Section 4.3.

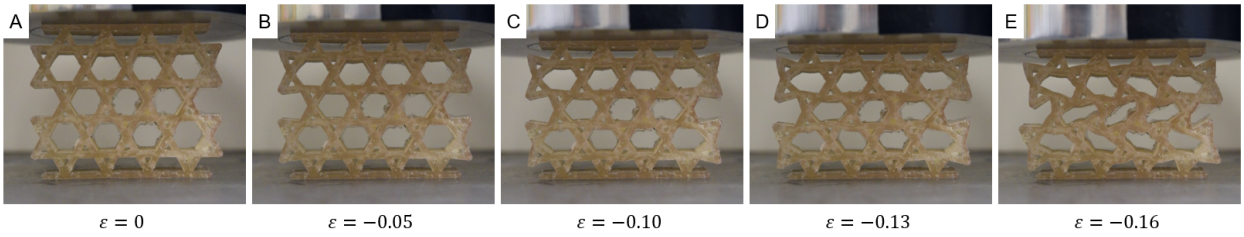

Figure 6.3: Compression of the Kagome PDMS-SP lattice. Onset of buckling occurs in D, at around -0.13 strain.

However, as shown in Figure 6.3, the lattice buckled to the side before activation strains could be reached. Buckling occurred around 0.13 compressive strain (Figure 6.4), so even with the 2x strain amplification provided by the Kagome structure, the internal principal strains were still far from the 0.7 strain required for spiropyran activation.

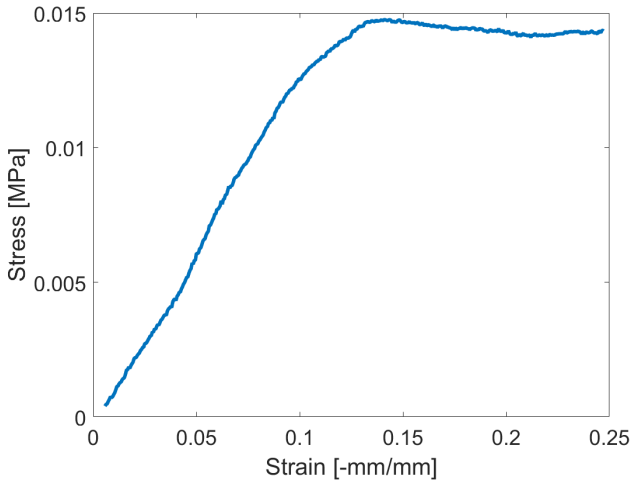

Figure 6.4: Stress-strain plot for the Kagome compression test.

Consequently, it was determined that the critical buckling strain of a truss-like lattice in compression would likely precede the activation strain of spiropyran. As other, more stretch-dominated structures have lower critical buckling strains than the Kagome lattice and bend-dominated structures do not amplify global strains to the same extent, other

lattice geometries must be considered to achieve mechanophore activation.

6.3 PDMS Oval Lattice - Compression

6.3.1 Selection of Oval Structure

As mentioned above, traditional lattice structures are faced with challenges like buckling when experiencing the extreme deformation required to activate spiropyran. Consequently, a pore-based structure, similar to the contact stiffening lattice, was adopted. The oval lattice consists of a patterns of oval holes in the material to act as stress/strain concentrators. As this lattice has more material, it does not buckle under compression.

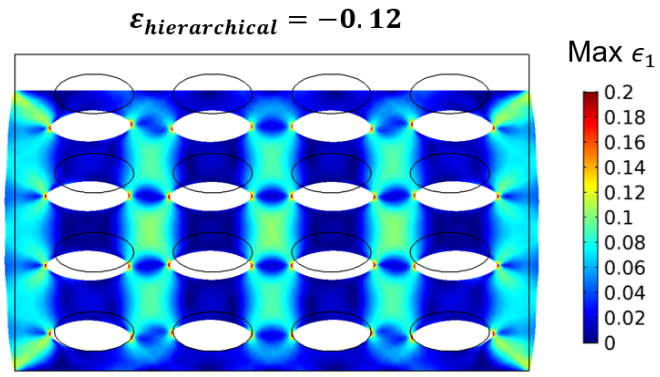

Figure 6.5: COMSOL model of the oval lattice in compression.

Simulation found that this structure amplifies the global strain applied to it by 2x, similar to the Kagome lattice (Figure 6.5). Using the same method as for the Kagome lattice described above, an oval lattice was created out of 15:1 PDMS with spiropyran and compressed at 20 mm/min on the Instron.

6.3.2 Experimental Results

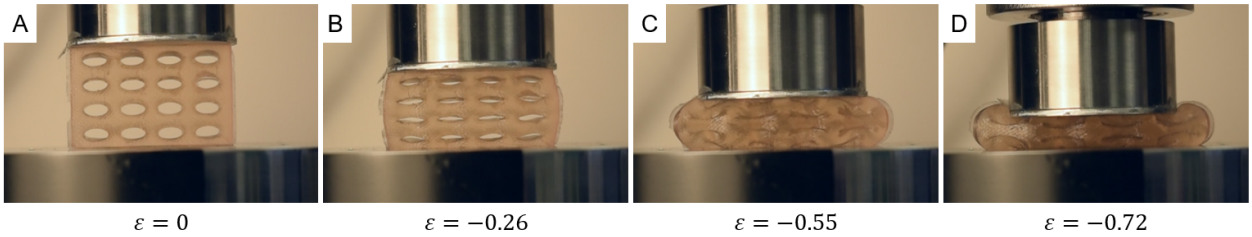

Figure 6.6: Compression of the PDMS-SP oval lattice.

Compression of the structure can be seen in Figure 6.6. Activation of spiropyran is thought to occur around between 0.5 and 0.6 compressive strain through video analysis; darkening in the central, high strain parts of the lattice can be seen in frame C. This color deepens and spreads throughout the compressed lattice (D) until it fractures (not pictured).

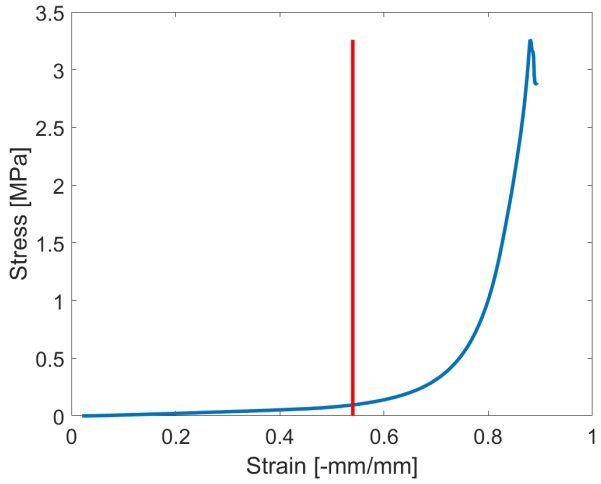

Figure 6.7: Stress-strain plot for the PDMS-SP oval lattice. The red line is where activation is estimated to occur, at 0.55 compressive strain.

As shown in Figure 6.7, the stress-strain behavior for the oval lattice in compression is similar to that of the bulk 15:1 PDMS though it is about a fifth as stiff. However,

activation has been triggered at around 0.5-0.6 compressive strain, instead of 0.7 as seen in the bulk quasi-static tests in Chapter 4. This indicates that pore-based lattices may enhance mechanophore activation while avoiding buckling problems.

6.4 PCL Oval Lattice - Tension

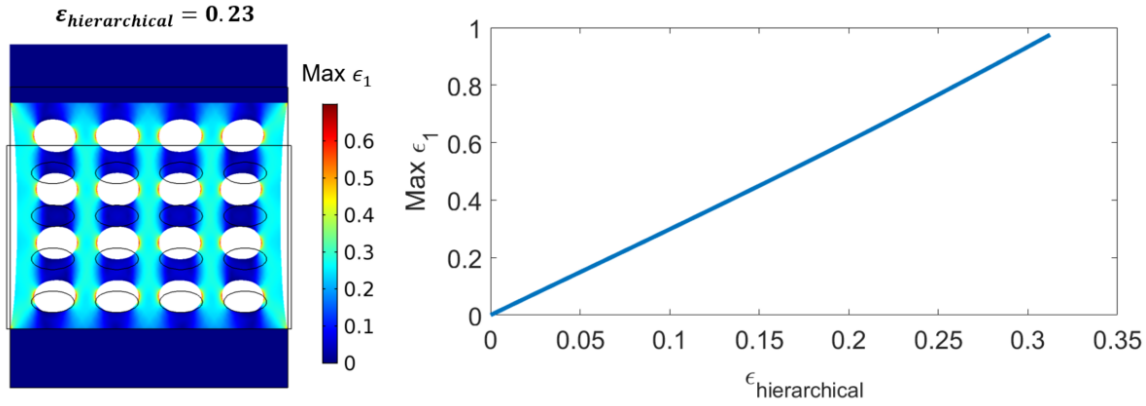

Figure 6.8: Right: COMSOL model of the oval lattice in tension. Left: Comparison of max principal strain vs. global ("hierarchical") strain for the oval lattice in tension.

Finally, the oval lattice was attempted in tension, as simulation suggested the oval stress concentrators could amplify strains as much as 3x when stretched apart (Figure 6.8). However, PDMS has little shear strength, so oval lattices and control samples were 3D printed in from spiroypran-embedded PCL using a fused-deposition printer on 100% infill.

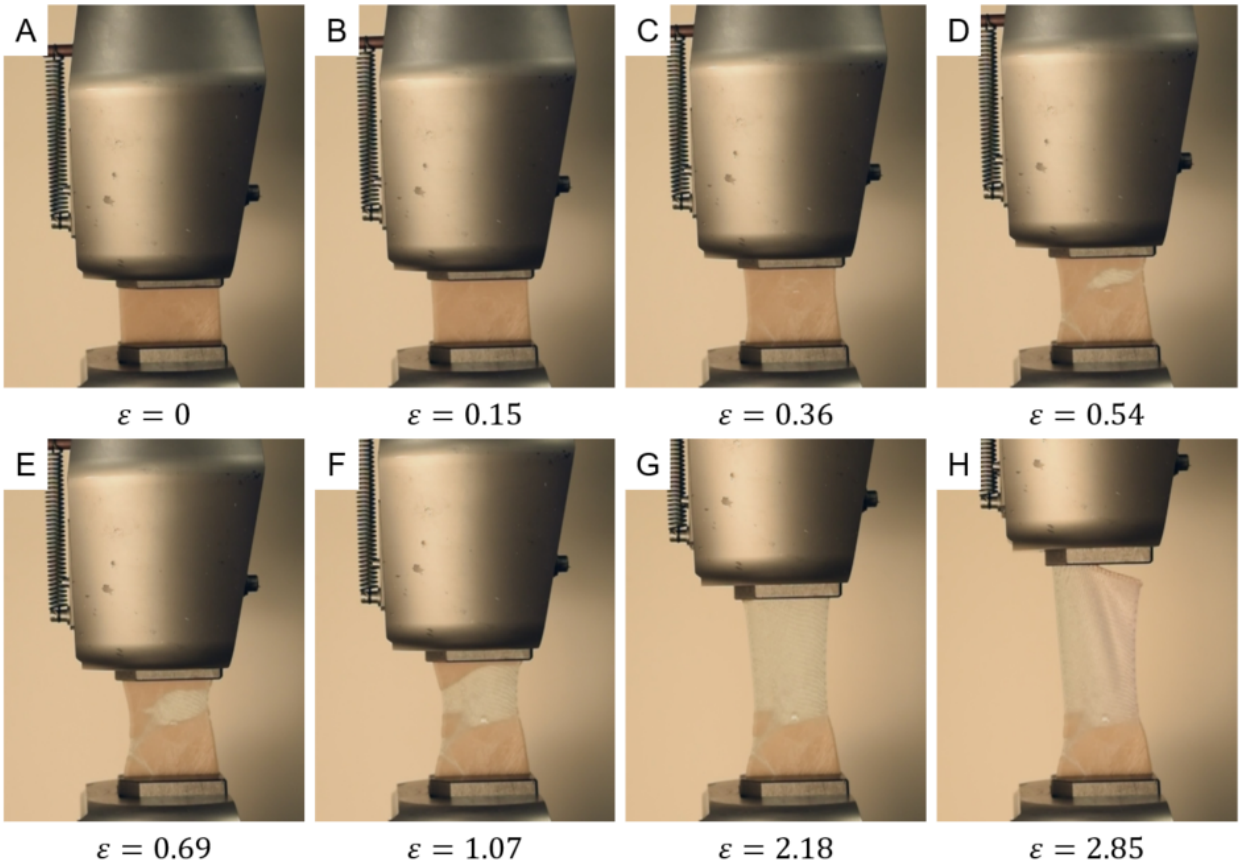

Figure 6.9: Frames from the video of the PCL-SP control loaded in tension. These images were white balance corrected using Adobe Premiere Pro.

Both the control samples and the lattices were then pulled apart at a rate of 20 mm/min on the Instron. Figure 6.9 shows a control print, measuring 48.6 mm wide, 1.9 mm thick and with an anvil height of 26.9 mm, undergoing the tensile test. The sample begins to separate around frame C, leading to the large tear in frame D. As the 3D printed fibers begin to shear against each other and stretch, the faint blue of activated spiropyran can be seen in subsequent frames (E-G). Finally, the sample slips from the grips and the spiropyran changes color from its active blue state to its active purple state (H). The stress-strain curve from this test can be seen in Figure 6.11 below.

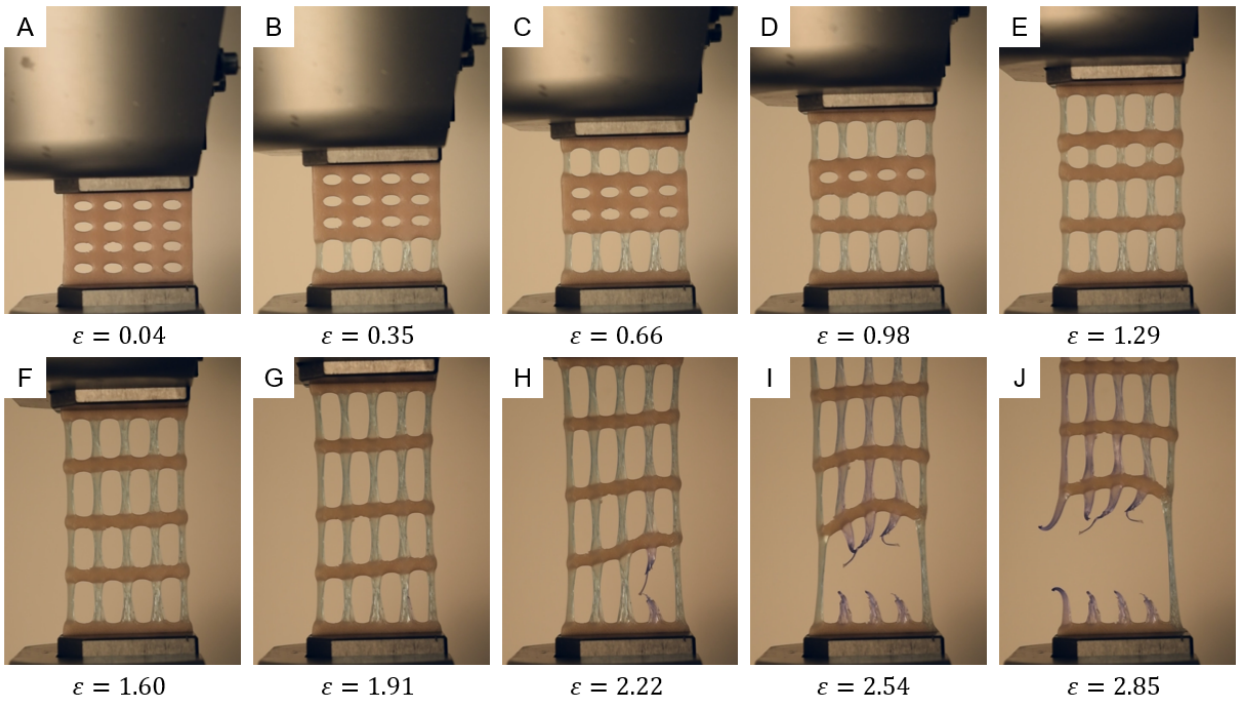

Figure 6.10: Frames from the video of the PCL-SP oval lattice loaded in tension. These images were color corrected in Adobe Premiere Pro.

Figure 6.10 shows the oval lattice, measuring 48.4 mm wide, 2.4 mm thick and with an anvil height of 32.1 mm, undergoing extreme elongation. During this test, the rows of the oval lattice failed one at a time, with the bottom row yielding first (B), followed by the top row (C), lower middle row (D) and then the upper middle row (E-F). The activated blue spiropyran can be seen in all row failures, as can its lower energy purple form in frames H-J following fracture.

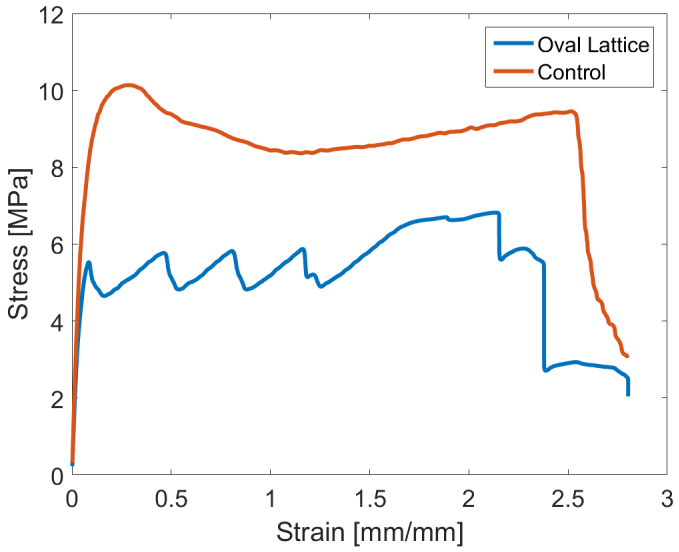

Figure 6.11: Stress-strain plots for the control and oval PCL lattices. Each of the peaks in the Oval Lattice curve correspond to a row failing.

When compared to a control sample of similar dimensions, the oval lattice was about half as strong (Figure 6.11). However, the control sample did not activate any sooner than 0.36 strain (when first separation of 3D printed fibers can be seen, Figure 6.9 C), while the oval lattice, through controlled failure of a row of ovals, first activated around 0.05-0.1 strain. It also repeated activating through the cascade of row failures. These results suggest that the oval geometry can also prematurely trigger mechanophore activation as it does in compression.

6.5 Conclusions

These preliminary results suggest that for typical truss-based lattice structures, spiropyran activation is difficult to achieve in compression due to the critical buckling strain of stretch-dominated structures likely being lower than the activation strain (0.7) required by the mechanophore. However, certain microstructures, such as an array of small pores in the bulk

material, may be used to trigger spiropyran activation earlier than it would occur in a bulk material. Compression testing of spiropyran-PDMS samples suggests that activation may be triggered before the critical strain of 0.7 due to internal oval geometry, and spiropyran-PCL oval samples in tension indicate activation certainly occurs before activation found in control samples. Future investigations could explore the competition between $\varepsilon_{critical}$ of buckling and $\varepsilon_{activation}$ for mechanophores, as well as optimizing small stress/strain concentrators (i.e. pore shapes) to enhance mechanophore activation.

BIBLIOGRAPHY

[1] V. F. Nesterenko, *Dynamics of Heterogenous Materials*. New York: Springer, 2001.

[2] M. F. Ashby, "The properties of foams and lattices," *Phil. Trans. Roy. Soc. A*, vol. 364, no. 1838, pp. 15–30, 2006.

[3] C. V. Jutte and S. Kota, "Design of nonlinear springs for prescribed load-displacement functions," *J. Mech. Des.*, vol. 130, no. 8, 2008.

[4] Q. Ma, H. Cheng, K. Jang, H. Luan, K. Hwang, J. A. Rogers, Y. Huang, and Y. Zhang, "A nonlinear mechanics model of bio-inspired hierarchical lattice materials consisting of horseshoe microstructures," *J. Mech. Phys. Solid*, vol. 90, pp. 179–202, 2016.

[5] F. Wang, O. Sigmund, and J. S. Jensen, "Design of materials with prescribed nonlinear properties," *J. Mech. Phys. Solids*, vol. 69, pp. 156–174, 2014.

[6] D. A. Davis, A. Hamilton, J. Yang, L. D. Cremar, D. V. Gough, S. L. Potisek, M. T. Ong, P. V. Braun, T. J. Martinez, S. R. White, J. S. Moore, and N. R. Sottos, "Force-induced activation of covalent bonds in mechanoresponsive polymeric materials," *Nature*, vol. 459, pp. 68–72, 2009.

[7] G. R. Gossweiler, G. B. Hewage, G. Soriano, Q. Wang, G. W. Welshofer, X. Zhao, and S. L. Craig, "Mechanochemical activation of covalent bonds in polymers with full and repeatable macroscopic shape recovery," *ACS Macro Lett.*, vol. 3, no. 3, pp. 216–219, 2014.

[8] J. R. Hemmer, P. D. Smith, M. van Horn, S. Alnemrat, B. P. Mason, J. R. de Alaniz, S. Osswald, and J. P. Hooper, "High strain rate-response of spiropyran mechanophores in PMMA," *J. Polym. Sci. Part B: Polym. Phys.*, vol. 52, 2014.

[9] G. I. Peterson, M. B. Larsen, M. A. Ganter, D. W. Storti, and A. J. Boydston, "3D-printed mechanochromic materials," *ACS Appl. Mater. Interfaces*, vol. 7, no. 1, pp. 577–583, 2015.

[10] M. B. Larsen and A. J. Boydston, "Successive mechanochemical activation and small molecule release in an elastomeric material," *J. Amer. Chem. Soc*, vol. 136, no. 4, pp. 1276–1279, 2014.

[11] A. L. Black Ramirez, Z. S. Kean, J. A. Orlicki, M. Champhekar, S. M. Elsakr, W. E. Krause, and S. L. Craig, "Mechanochemical strengthening of a synthetic polymer in response to typically destructive shear forces," *Nature Chem*, vol. 5, pp. 757–761, 2013.

[12] U. G. K. Wegst, H. Bai, E. Saiz, A. P. Tomsia, and R. O. Ritchie, "Bioinspired structural materials," *Nature Materials*, vol. 14, pp. 23–36, 2015.

[13] X. Zheng, H. Lee, T. H. Weisgraber, M. Shusteff, J. DeOtte, E. B. Duoss, J. D. Kuntz, M. M. Biener, Q. Ge, J. A. Jackson, S. O. Kucheyev, N. X. Fang, and C. M. Spadaccini, "Ultralight, ultrastiff mechanical metamaterials," *Science*, vol. 344, no. 6190, pp. 1373–1377, 2014.

[14] V. Deshpande, M. Ashby, and N. Fleck, "Foam topology: bending versus stretching dominated architectures," *Acta Mater.*, vol. 49, no. 6, pp. 1035–1040, 2001.

[15] P. Li, Z. Wang, N. Petrinic, and C. R. Siviour, "Deformation behaviour of stainless steel microlattice structures by selective laser melting," *Mat. Sci. Eng. A.*, vol. 614, pp. 116–121, 2014.

[16] M. Smith, Z. Guan, and W. J. Cantwell, "Finite element modelling of the compressive response of lattice structures manufactured using the selective laser melting technique," *Int. J. Mech. Sci.*, vol. 67, pp. 28–41, 2013.

[17] T. A. Schaedler, A. J. Jacobsen, A. Torrents, A. E. Sorensen, J. Lian, J. R. Greer, L. Valdevit, and W. B. Carter, "Ultralight metallic microlattices," *Science*, vol. 334, no. 6058, pp. 962–965, 2011.

[18] B. Haghpanah, H. Ebrahimi, D. Mousanezhad, J. Hopkins, and A. Vaziri, "Programmable elastic metamaterials," *Adv. Eng. Mater.*, vol. 18, no. 4, pp. 643–649, 2016.

[19] J. T. B. Overvelde and K. Bertoldi, "Relating pore shape to the non-linear response of periodic elastomeric structures," *J. Mech. Phys. Solids*, vol. 64, pp. 351–366, 2014.

[20] F. Fraternali, G. Carpentieri, A. Amendola, R. E. Skelton, and V. F. Nesterenko, "Multiscale tunability of solitary wave dynamics in tensegrity metamaterials," *Appl. Phys. Lett.*, vol. 105, no. 201903, 2014.

[21] J. R. Raney, N. Nadkarni, C. Daraio, D. M. Kochmann, J. A. Lewis, and K. Bertoldi, "Stable propagation of mechanical signals in soft media using stored elastic energy," *Proc. Nat. Academy Sci.*, vol. 113, no. 35, 2016.

[22] Stratasys, "3d printing with rubber-like material." `http://www.stratasys.com/materials/polyjet/rubber-like`, 2017. online: accessed Apr 5 2017.

[23] S. H. Kang, S. Shan, A. Kosmrlj, W. L. Noorduin, S. Shian, J. C. Weaver, D. R. Clarke, and K. Bertoldi, "Complex ordered patterns in mechanical instability induced geometrically frustrated triangular cellular structures," *Phys. Rev. Lett.*, vol. 112, 2014.

[24] M. P. Bendsoe and O. Sigmund, *Topology Optimization.* Berlin: Springer, 2003.

[25] E. Andreassen, A. Clausen, M. Schevenels, B. S. Lazarov, and O. Sigmund, "Efficient topology optimization in MATLAB using 88 lines of code.," *Struct. Mult. Opt.*, vol. 43, no. 1, pp. 1–16, 2011.

[26] H. C. Gea and J. Luo, "Topology optimization of structures with geometric nonlinearities," *Computers and Structures*, vol. 79, no. 20–21, pp. 1977–1985, 2001.

[27] T. E. Bruns and D. A. Tortorelli, "Topology optimization of non-linear elastic structures and compliant mechanisms," *Comput. Methods Appl. Mech. Eng.*, vol. 190, no. 26-27, pp. 3443–3459, 2001.

[28] J. Wu, C. Dick, and R. Westermann, "A system for high-resolution topology optimization," *IEEE Trans. Vis. Comp. Graphics*, vol. 22, no. 3, pp. 1195–1208, 2016.

[29] MathWorks, "Genetic algorithm." `https://www.mathworks.com/discovery/genetic-algorithm.html`, 2017. online: accessed Mar 27 2017.

[30] COMSOL, "LiveLink for MATLAB user's guide," 2012. Version 4.3.

[31] MathWorks, "ga: Find minimum of function using genetic algorithm." `https://www.mathworks.com/help/gads/ga.html`, 2017. online: accessed Mar 29 2017.

[32] C. M. Kingsbury, P. A. May, D. A. Douglas, S. R. White, J. S. Moore, and N. R. Sottos, "Shear activation of mechanophore-crosslinked polymers," *J. Mater. Chem*, vol. 48, pp. 1335–1342, 2015.

[33] J. W. Kim, Y. Jung, G. W. Coates, and M. N. Silberstein, "Mechanoactivation of spiropyran covalently linked PMMA: Effect of temperature, strain rate, and deformation mode," *Macromolecules*, vol. 48, no. 5, 2015.

[34] Z. Wang, "Polydimethylsiloxane mechanical properties measured by macroscopic compression and nanoindentation techniques," Master's thesis, University of South Florida, 3 2011.

[35] M. E. Grady, B. A. Beiermann, J. S. Moore, and N. R. Sottos, "Shockwave loading of mechanochemically active polymer coatings," *ACS Appl. Mater. Interfaces*, vol. 6, no. 8, pp. 5350–5335, 2014.

Appendix A

PDMS SAMPLE PREPARATION

A.1 Introduction

Polydimethylsiloxane (PDMS) is an inert, clear silicone that we use as a substrate for studying surface wave propagation and mechanophore activation. To make our samples, we use Dow Corning's Sylgard 184 Silicone Elastomer Kit, which comes as a two-part liquid kit, containing a viscous base and a thinner curing agent. PDMS behaves viscoelastically under loading, and its stiffness can be controlled by the base:curing agent ratio, where a 10:1 mixture will yield a stiff, shape-holding material, while a 40:1 ratio will result in jello-esque characteristics. When the base and curing agent are mixed together, the resulting PDMS mixture has a pot life of about 30 minutes before it will set in its mold. This instruction sheet describes the mixing and molding process.

A.2 Personal Protective Equipment (PPE)

Before starting the mixing/molding process, one should **read the MSDS** for PDMS. While safety precautions are discussed here and in the procedure below, it is essential to understand all risks when starting a new chemical procedure.

A.2.1 PDMS Base

The base material is very stable under normal conditions and classified as a nontoxic substance. However, wearing safety glasses and washing hands after contact with the liquid is recommended.

A.2.2 PDMS Curing Agent

The PDMS curing agent has a Category 2 warning for reproductive toxicity. Consequently, it is required that safety glasses and gloves are used for handling this substance.

A.3 Storage and Clean-Up

Both the base and curing agent are stored in the polymer cabinets in the AERB lab beneath the fume hood. Empty base or curing agent containers should be marked as such and removed/thrown out as soon as possible. Any extra base + curing agent + spiropyran should be poured into the container labeled "PDMS WASTE" in the fume hood and left to cure, while the mixing cup should be thrown in the trash.

A.4 Procedure

Figure A.1: Required equipment for producing PDMS cube samples.

Below are the steps to create PDMS cubes with and without spiropyran.

1. Gather the supplies shown in Figure A.1. This includes:

    - 0.5" Width Kapton Tape
    - Scissors
    - PDMS base and curing agent
    - Mixing cup
    - Balance
    - Square aluminum mold(s)
    - Plastic petri dish(es)
    - Gloves
    - Mold release
    - Acetone
    - Kim wipes
    - Hand mixer

    Don the gloves and, if desired, an apron.

2. With the kim wipes and acetone, wipe down the petri dishes, molds and whisk on the mixer. Clean until any previous remnants of PDMS are removed and that the molds and dishes are free of impurities like dust or old spiropyran.

3. Tare the scale with the mixing cup on it.

4. Add volume of the PDMS base to the mixing cup (shown below). In order to fill all three of the small aluminum molds, 90 grams of the base are required.

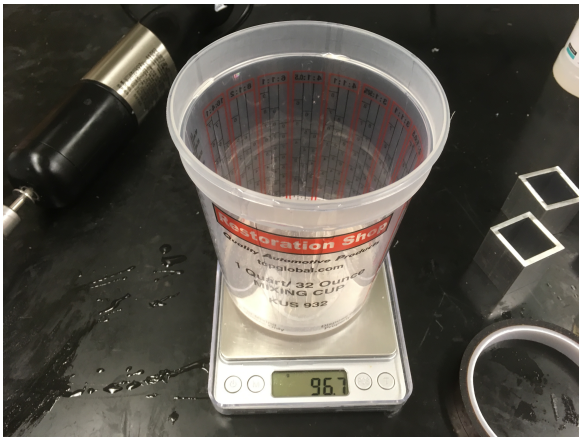

Figure A.2: Weighing the base agent.

5. Tare the scale again and then add the appropriate amount of curing agent BY WEIGHT to the mixing cup. All samples in this thesis were 15:1, so using the 90 g value of base material, this means that 6.0 g of curing agent are added.

6. For samples with spiropyran, add 1.56 mg of spiropyran per gram of base to the sample. Spiropyran is often kept in a 0.1 g/mL suspension of xylenes. So, for 90 g of base material:

$$\frac{1 \text{ mL [Xylenes]}}{0.1 \text{ g [SP]}} * \frac{1.56 \text{ mg [SP]}}{1.0 \text{ g [Base]}} * 90 \text{ g [Base]} = 1.4 \text{ mL [Xylenes]}$$

Using a syringe, withdraw the spiropyran-xylene solution from the vial (in this case, 1.4 mL of solution), tightly capping the container when finished. Next, empty the syringe through the cotton filter into the PDMS mixing container.

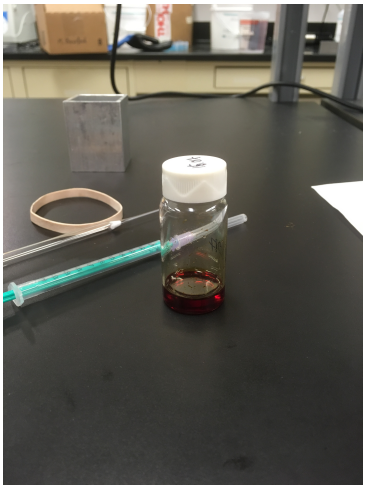

Figure A.3: Spiropyran with accompanying syringe and cotton filter.

7. Using the hand mixer, mix the PDMS base, curing agent and spiropyran together until it is an even gold-brown color.

8. Place the mixing container in the vacuum chamber in the fume hood and start the vacuum to begin removing bubbles in the mixture. Periodically check on the container and release the vacuum, allowing the re-pressurization to pop the bubbles.

9. While the vacuum is running, use the kapton tape to tape the aluminum molds tightly to the petri dishes as shown below:

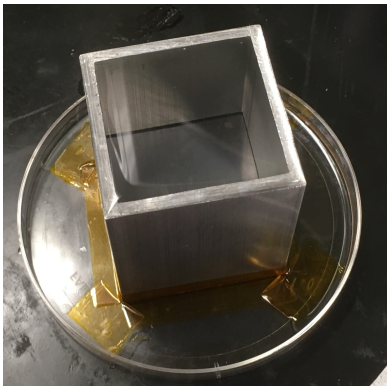

Figure A.4: Mold filled with bubble-free PDMS mixture.

10. Spray mold release on the inside of the molds. Ensure that it finds the corners of the molds.

11. Pour the bubble-free PDMS mixture into the molds until they are completely filled.

12. Re-vacuum the PDMS-filled molds as necessary to remove any bubbles introduced into the mixture by the pouring process.

13. Place PDMS molds into oven set to 60deg C for at least four hours. PDMS may be cured overnight as well.

14. Dispose of excess mixture in the "PDMS Waste" container in the fume hood and place soiled gloves, mixing bowls, etc. in the trahs.

15. Post-curing, carefully pull the aluminum molds from the petri dishes and then push the cured PDMS free from the aluminum. Samples without spiropyran will be optically clear, while spiropyran samples will adopt the gold-brown color of spiropyran, as seen in the photo below:

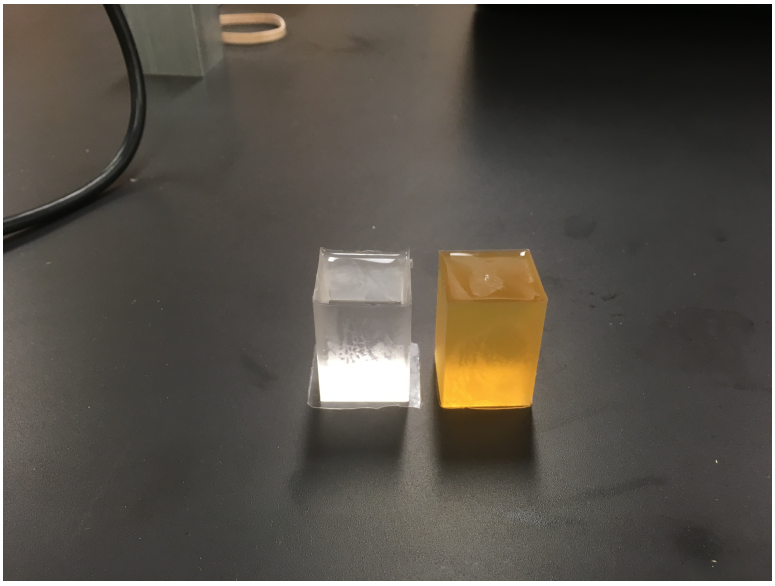

Figure A.5: Comparison between control (left) and spiropyran cube samples (right).

Appendix B

TOPOLOGY OPTIMIZATION CODE

B.1 Main

```
close all; clc
clear all
%%
%==== User Input ====
tic
msize = 10; % Set optimization matrix size
A_initial = ones(1,msize^2);

% Set forces for: narrow i-beam [displacement (cm) force (N)]
targets = [
0.0000   0.0000
0.20000  739.65
0.40000  1474.3
0.60000  2203.9
0.80000  2928.6
1.0000   3648.3
1.2000   4363.0
1.4000   5072.8
1.6000   5777.7
```

```
20 1.8000   6477.7
21 2.0000   7172.7];
22
23 csvwrite('Targets.dat',targets) %vWrite targets to txt file
24
25 %%
26 %===== Run Code =====
27 % tic
28 display('Caution: Optimizing in process...')
29
30 % Vector length of reshaped matrix A
31 s = msize^2;
32
33 LB = zeros(1,s); % Vector of lower bounds (size x 1)
34 UB = ones(1,s); % Vector of upper bounds (size x 1)
35
36 % Enforce GA to give you integers for these indices
37 IntCon = [1:1:s]';
38
39 options = gaoptimset('UseParallel',false, ...
40     'FitnessLimit',100,'TimeLimit',600000000, 'StallTimeLimit'
        ,600000000, ...
41     'StallGenLimit', 30, 'TolFun',1,'InitialPopulation',A_initial,
        ...
42     'PlotFcns',{@gaplotbestf,@gaplotstopping},'PopulationSize',50,
        ...
```

```
43      'Generations',50);
44  [x,fval,exitflag,output,population,scores]  ...
45      = ga(@COMSOL_Interface3,s,[],[],[],[],LB,UB,@GA_filter3,IntCon
            ,options);
46
47  toc % Time computation
```

B.2 GA Filter

```
1   function [c, ceq] = GA_filter3(x)
2
3   persistent f_count;
4   if isempty(f_count), f_count = 0; end
5   f_count = f_count + 1; % Count how many solutions have been
       attempted
6
7   if mod(f_count,10)==0
8   display(['F_Counter = ' num2str(f_count)]);
9   assignin('base','f_count',f_count) % Display every 10th number of
       solutions
10  end
11
12  A_size = sqrt(length(x));
13
14  A = reshape(x,A_size,A_size)';
15
16  c = zeros(4,1);
```

```
c(1,1) = [A_size - sum(A(1,:))]; % Enforce top solid edge
c(2,1) = [A_size - sum(A(end,:))]; % Enforce top solid edge
CC = bwconncomp(A);
if CC.NumObjects > 1, c(3,1) = 1; end % Check if single body
ceq = [];
```

B.3 COMSOL Interface

```
function [T] = COMSOL_Interface3(A)

persistent counter;
if isempty(counter), counter = 0; end
counter = counter + 1;
assignin('base','Comsol_called',counter) % Display how many times
   COMSOL has been called

persistent targets;
if isempty(targets)
    targets = csvread('C:\Users\Boechler Lab Comp 3\Documents\
       COMSOL_11Mar\Targets.dat'); % Find target force-
       displacement values if not in memory
end

l = length(A);
size = sqrt(l);
A = reshape (A,size,size)';

```

```
17 [f] = fea_build_block(A); % Call FEA Build
18
19  T = sum(abs(targets(:,2)-f(:,2))); % Fitness function
```

B.4 FEA Build

```
1
2 function out = fea_build_block(A)
3
4 try
5
6 % Set design domain dimensions to 1 m x 1 m
7 ymax = 1;
8 xmax = 1;
9 ymin = 0;
10 xmin = 0;
11
12 % Set tolerance for selection boxes
13 tol = .05;
14
15 % Create model from matrix A
16
17 A = flipud(A);
18
19 % Make the model
20
21 import com.comsol.model.*
```

```
22 import com.comsol.model.util.*
23 model = ModelUtil.create('model');
24
25 % Create a 2D model geometry
26 model.geom.create('geom1',2);
27
28 % Start by building a 1m x 1m block positioned at (0,0)
29 model.geom('geom1').feature.create('r0','Rectangle');
30 model.geom('geom1').feature('r0').set('size',{'1' '1'});
31 model.geom('geom1').feature('r0').set('pos',{'0' '0'});
32
33 % Define the size of the rectangle based on the size of A
34 dx = 1/size(A,1);
35 dy = 1/size(A,2);
36
37 % Initialize the x and y positions
38 ypos = 0;
39 xpos = 0;
40 n_rect = 0;
41
42 % Run through a for loop to delete A = 0 blocks. This creates
     structure
43 % from A matrix.
44 for n = 1:size(A,2)
45     for m = 1:size(A,1)
46         % If this value of A is 0, take the chunk out
```

```
47          if ~A(m,n)
48              n_rect = n_rect+1;
49              rect_str = ['model.geom(''geom1'').feature.create(''r'
                    num2str(n_rect) ''',''Rectangle'');'];
50              size_str = ['model.geom(''geom1'').feature(''r'
                   num2str(n_rect) ''').set(''size'',{''' num2str(dx)
                   ''' ''' num2str(dy) '''});'];
51              pos_str =  ['model.geom(''geom1'').feature(''r'
                   num2str(n_rect) ''').set(''pos'',{''' num2str(xpos)
                    ''' ''' num2str(ypos) '''});'];
52              eval(rect_str); eval(size_str); eval(pos_str);
53          end
54
55          % Reposition the rectangle in x
56          ypos = ypos + dy;
57      end
58
59      % Go to the next row up
60      xpos = xpos + dx;
61
62      % Start at the left again for the next row
63      ypos = 0;
64  end
65
66  % If there are rectangles to be cleared
67  if n_rect
```

```
68      % Make the difference
69      model.geom('geom1').feature.create('dif1','Difference');
70      % Set the large block as the positive part
71      model.geom('geom1').feature('dif1').selection('input').set({'
            r0'});
72
73      % Make a string of all the rectangles to delete
74      inp_str = [];
75      inp_str =  ['model.geom(''geom1'').feature(''dif1'').selection
            (''input2'').set({'];
76      for k = 1:n_rect
77          inp_str = [inp_str '''r' num2str(k) ''' ' ];
78      end
79      inp_str = [inp_str '});'];
80
81      % Evaluate the deletion string
82      eval(inp_str);
83  end
84
85  % Build the geometry
86  model.geom('geom1').run;
87
88  A = flipud(A);
89
90
91  % Create the solid mechanics model
```

```
92 model.physics.create('solid', 'SolidMechanics', 'geom1');
93
94 % Create the study
95 model.study.create('std1');
96 model.study('std1').create('stat', 'Stationary');
97 model.study('std1').feature('stat').activate('solid', true);
98
99 % Set the material and properties
100 model.material.create('mat1', 'Common');
101 model.material('mat1').label('TangoBlack');
102 model.material('mat1').propertyGroup('def').set('density', '1.14[g
    /cm^3]');
103 model.material('mat1').propertyGroup.create('Enu', 'Young''s
    modulus and Poisson''s ratio');
104 model.material('mat1').propertyGroup('Enu').set('poissonsratio', '
    0.4');
105 model.material('mat1').propertyGroup('Enu').set('youngsmodulus', '
    6.95e5[Pa]');
106 model.material('mat1').set('family', 'plastic');
107
108 % Select whole domain boundary
109 model.selection.create('whole', 'Box');
110 model.selection('whole').set('xmin', xmax/2-1);
111 model.selection('whole').set('ymin', ymax-2);
112 model.selection('whole').set('xmax', xmax/2+1);
113 model.selection('whole').set('ymax', ymax+2);
```

```
model.selection('whole').set('condition','intersects');
model.selection('whole').set('entitydim','2');
model.geom('geom1').run;

%Plotting
figure(10)
mphgeom(model,'geom1');
drawnow

top = mphselectbox(model,'geom1',[xmin-tol xmax+tol; ymax-tol ymax
    +tol], 'boundary');

bottom = mphselectbox(model,'geom1',[xmin-tol xmax+tol; ymin-tol
    ymin+tol], 'boundary');

% Set COMSOL simulation
model.physics('solid').prop('d').set('d', '1 [m]');
model.physics('solid').feature.create('fix1', 'Fixed', 1);
model.physics('solid').feature('fix1').selection.set(bottom);
model.physics('solid').feature.create('disp1', 'Displacement1', 1)
    ;
model.physics('solid').feature('disp1').selection.set(top);
model.physics('solid').feature('disp1').setIndex('Direction', true
    , 0);
model.physics('solid').feature('disp1').setIndex('Direction', true
    , 1);
```

```
135 model.physics('solid').feature('disp1').setIndex('U0', '-dy', 1);
136
137 % Set mesh
138 mesh1 = model.mesh.create('mesh1','geom1');
139 mesh1.feature.create('frt1','FreeTri');
140 mesh1.run;
141
142 % Define COMSOL study and constraintss
143 model.study('std1').create('param', 'Parametric');
144 model.study('std1').feature('param').set('showdistribute', false);
145 model.study('std1').feature('param').setIndex('pname', 'dy', 0);
146 model.study('std1').feature('param').setIndex('plistarr', 'range
    (0,.2,2)', 0);
147 model.study('std1').feature('param').setIndex('punit', 'cm', 0);
148 model.study('std1').feature('stat').set('showdistribute', false);
149 model.study('std1').feature('stat').set('geometricNonlinearity', '
    on');
150
151 model.sol.create('sol1');
152 model.sol('sol1').study('std1');
153
154 model.study('std1').feature('stat').set('listsolnum', 1);
155 model.study('std1').feature('stat').set('solnum', '1');
156
157 % Create parametric sweep
158 model.sol('sol1').create('st1', 'StudyStep');
```

```
159 model.sol('sol1').feature('st1').set('study', 'std1');
160 model.sol('sol1').feature('st1').set('studystep', 'stat');
161 model.sol('sol1').create('v1', 'Variables');
162 model.sol('sol1').feature('v1').set('control', 'stat');
163 model.sol('sol1').create('s1', 'Stationary');
164 model.sol('sol1').feature('s1').create('p1', 'Parametric');
165 model.sol('sol1').feature('s1').feature('p1').set('pname', {'dy'})
      ;
166 model.sol('sol1').feature('s1').feature('p1').set('plistarr', {'
      range(0,.2,2)'});
167
168 model.sol('sol1').feature('s1').feature('p1').set('punit', {'cm'})
      ;
169 model.sol('sol1').feature('s1').feature('p1').set('sweeptype', '
      sparse');
170 model.sol('sol1').feature('s1').feature('p1').set('preusesol', 'no
      ');
171 model.sol('sol1').feature('s1').feature('p1').set('
      pcontinuationmode', 'no');
172 model.sol('sol1').feature('s1').feature('p1').set('plot', 'off');
173 model.sol('sol1').feature('s1').feature('p1').set('plotgroup', '
      Default');
174 model.sol('sol1').feature('s1').feature('p1').set('probesel', 'all
      ');
175 model.sol('sol1').feature('s1').feature('p1').set('probes', {});
176 model.sol('sol1').feature('s1').feature('p1').set('control', '
```

```
    param');
model.sol('sol1').feature('s1').set('control', 'stat');
model.sol('sol1').attach('std1');

model.sol('sol1').runAll;

model.result.numerical.create('int1', 'IntLine');
model.physics('solid').feature('fix1').selection.set(bottom);

% Extract force-displacement data
model.result.numerical('int1').selection.set(bottom);
model.result.numerical('int1').set('expr', 'solid.RFy');
model.result.table.create('tbl1', 'Table');
model.result.table('tbl1').comments('Line Integration 1 (solid.RFy
    )');
model.result.numerical('int1').set('table', 'tbl1');
model.result.numerical('int1').setResult;
tabl = mphtable(model,'tbl1');
out = tabl.data

% Count how many solutions are successfully solved in COMSOL
persistent fea_success;
if isempty(fea_success), fea_success = 0; end
fea_success = fea_success +1;

assignin('base','fea_success',fea_success)
```

```
201
202 ModelUtil.clear; % Clear COMSOL model
203 catch ME
204     ME
205 end
206 end
```